DEVELOPMENT OF A NOVEL DEVICE FOR HEMOSTATIC POWDER DELIVERY TREATING GASTROINTESTINAL BLEEDINGS

by

Angelos Mavroudis

B.A., The University of British Columbia, 2023

A THESIS SUBMITTED IN PARTIAL FULFILLMENT OF

THE REQUIREMENTS FOR THE DEGREE OF

MASTER OF APPLIED SCIENCE

in

THE FACULTY OF GRADUATE AND POSTDOCTORAL STUDIES

(Mechanical Engineering)

THE UNIVERSITY OF BRITISH COLUMBIA

(Vancouver)

October 2023

The following individuals certify that they have read and recommend to the Faculty of Graduate and Postdoctoral Studies for acceptance the thesis entitled:

Development of a novel device for hemostatic powder delivery treating gastrointestinal bleedings

submitted by Angelos Mavroudis in partial fulfillment of the requirements for

the degree of Master of Applied Science

in Mechanical Engineering

Examining Committee:

Dana Grecov, Professor, Mechanical Engineering, UBC
Supervisor

Boris Stoeber, Professor, Mechanical Engineering, UBC
Supervisory Committee Member

Mu Chiao, Professor, Mechanical Engineering, UBC
Supervisory Committee Member

Abstract

Severe gastrointestinal hemorrhaging presents a complex challenge that can lead to potentially fatal outcomes. Although existing medical solutions offer some assistance in managing internal bleeding, they are unreliable due to their limitations. Recent work on innovative hemostatic powders has shown promising results in effectively controlling bleeding without imposing any risk to the patient. However, to efficiently deliver this hemostatic agent, an optimized delivery system is required. The hemostatic powder is characterized by adhesive properties that negatively impact its flowability. This research aims to create a prototype of a medical device to test and improve the flow of an adhesive hemostatic powder through a 0.002 m in diameter and 1.47 m in length catheter.

A detailed experimental analysis is performed to understand which parameters and how they affect the performance of the delivery system. In the experiments, the performance of the delivery system is characterized based on the delivery time and the powder mass deposition at the outlet of the catheter. A high-velocity gas flow is responsible for transporting the powder through a catheter and into a sealed container. A pressure regulator regulates the maximum pressure of the system at 68 kPa (10 psi), while the flow rate is adjusted using a gas flow regulator. Three different flow rates are examined in the experimental part of this work: 0.37 m^3/h, 0.31 m^3/h, and 0.23 m^3/h. Furthermore, to improve the device, different designs are being tested. The effects of dimensional changes on powder flowability are being examined with respect to the efficiency of powder delivery through the catheter.

A primary modeling approach for turbulent and dense gas-solid multiphase flows is being presented using computer-aided engineering. Computational fluid dynamics (CFD) and discrete

element methods (DEM) are combined to develop a computational model of the granular flow. This model is defined by specific attributes of the powder and the carrying fluid. The numerical results verification is supported by experimental data.

.

Lay Summary

For many years, the study of granular material behavior has been the focus of food and agricultural companies. The optimization of their transportation and storage was the goal of many engineering studies. In recent years, granular flows have been used by the medical industry, with the most common example being the inhaler. A medicinal powder must be delivered efficiently to a patient to prevent symptoms. In order to do that and manufacture optimized medical devices, the effects of different flow conditions must be studied. These conditions include the gas medium flow rate and the powder mass flow rate. In this work, using numerical simulations, the effect of various mass flow rates on powder was examined and characterized, while the verification of the numerical results was conducted using experiments.

Preface

Dr. Dana Grecov and researchers from the Kastrup Lab provided the identification and idea for this project.

The work presented in this report was done by me, except for Chapter 3.

In Chapter 3, the initial idea for the design of the device was created by Dr. Amin Arefi. Further modifications and improvements to the final device that was used during the experiments were performed by me and Dr. Amin Arefi.

Table of Contents

List of Tables

List of Figures

List of Symbols

a $angle$

a_f $fluid\ volume\ fraction$

a_i $particle\ \ or\ solid\ volume\ fraction$

A_p $particle\ surface\ area$

A_{sph} $surface\ area\ of\ a\ sphere\ of\ equivalent\ volume\ as\ the\ particle$

C_D $drag\ coefficient$

C_{D_E} $drag\ coefficient\ by\ Ergun$

C_{D_W} $drag\ coefficient\ Wen\ and\ Yu$

E_b $Young's\ Modulus\ for\ particles$

E_p $Young's\ Modulus\ for\ particles$

F_c $contact\ forces$

$F_{f\to p}$ $fluid-solid\ particle\ interaction\ forces$

F_n^t $normal\ contact\ forces$

$F_n^{t-\Delta t}$ $normal\ contact\ forces\ at\ the\ previous\ timestep$

$F_{n,adh}$ $adhesive\ contact\ force$

F_{p-f} $particle-fluid\ interaction\ force$

F_τ $tangential\ force$

$F_{\nabla p}$ $pressure\ gradient\ force$

g $gravitational\ acceleration$

h $height$

$\mathbb{I}$ $unit\ tensor$

K_{nl} *loading stiffness during particle collision*

$K_{nl,b}$ *loading stiffness for boundary*

$K_{nl,p}$ *loading stiffness for particles*

K_{nu} *unloading stiffness during particle collision*

L *particle size*

m_g *gas mass flowrate*

m_p *particle mass*

p *pressure*

r *radius*

r_{adh} *ratio of adhesive stiffness to contact loading stiffness*

Re_p *Reynolds number with respect to particle*

s_n^t *overlap between two solid particles*

$s_n^{t-\Delta t}$ *overlap between two solid particles at the previous time step*

$\dot{s}_\tau$ *tangential relative velocity vector*

$\mathbb{T}_f$ *stress tensor*

v_p *particle velocity*

$\dot{V}_g$ *gas volumetric flow rate*

δ_{adh} *adhesive distance*

ε *coefficient of restitution*

Θ *angle of wall inlcination*

λ *dimensionless constant regulating the effects of contact forces*

μ *friction coefficient*

μ_d $dynamic\ friction\ coefficient$

μ_s $static\ friction\ coefficient$

ρ_f $fluid\ density$

φ $particle\ sphericity$

ψ $blending\ parameter$

Acknowledgements

I offer my sincere gratitude to my two wonderful supervisors professor Dana Grecov and professor Savvas Hatzikiriakos for accepting me to this amazing two-year program and kept supporting and helped me push forward throughout its duration.

Also, I would like to thank our laboratory supervisor, Akshai Bose, for his support throughout my research.

Special thanks to our co-workers at Kastrup Lab who made this amazing powder. It is because of their brilliance that this project even exists.

Finally, I would like to thank my family and friends who supported me through thick and thin and helped me chase my dreams 10 thousand kilometers away from home.

Dedication

To my friends and family

Chapter 1: Introduction

1.1 Motivation

In the United States of America, 67-102 per 100,000 people are hospitalized annually due to upper gastrointestinal bleeding (UGIB), as reported in the work of Longstreth [8] and Wuerth et al. [9]. It is stated that UGIB cases increase with respect to age; more specifically, the chance of exhibiting gastrointestinal bleeding increases by 30-fold between the ages of 30-90 [8]. Like every disease, UGIB can also be characterized by its severity. The most life-threatening scenario is also referred to as acute upper gastrointestinal bleeding, with a mortality rate of 3-14% a percentage that has not changed in the last few years, as Leerdman states [2]. The mortality percentile can increase depending on the patient's admission to the hospital and age. Reportedly, patients of older age tend to develop acute gastrointestinal bleeding even after admission, and in those cases, the mortality rate reaches 25%. While there are currently few methods of treating UGIB, such as blood transfusion, antibiotics, or surgery, there is a chance of treatment complications, such as respiratory distress or infections [10]. A recent study introduced a new method for treating UGIB using hemostatic powder [5]. The most important parameter behind the usage of hemostatic powder, instead of the other more popular treatment methods, is the low complication risk after and during the surgical procedure. The most efficient way to use this hemostatic material is to apply it directly to the affected area and let it rest for a few seconds [15].

The key element of effectively administering the hemostatic powder is understanding the granular flow of the system. The study of granular flows fascinated many engineers due to the complexity of their nature [16] [17].

A plethora of studies over the past few decades have focused on analyzing the different parameters that might affect the flowability of the granular material. For example, Kesava et al. [17] in their book analyze the effects of interparticle behavior, boundary conditions, and hopper geometry on material flowability, proving the difficulty of an analytical granular flow calculation. Teunou et al. [18] revisited the effects of time consolidation on powder flowability that were first introduced by Jenike [19]. In their work, they studied the effects of storage time and time consolidation on various food-based granular materials. They showed that time consolidation, which is the time under which the granular material is subjected to compressive stress that appears due to gravitational forces, greatly impacts powder flowability. More specifically, the more time a granular material is stored, the less flowable it becomes.

Recent developments in medicine led to the production of medicinal powders used in dry powder inhalers [12] [13] [15]. This new type of granular material has opened a new path for granular model applications and studies. An important parameter that differentiates medical applications from food or plastic ones is the size of the domain where the flow develops, as well as the volume of particles that are transported. For example, in the food industry, the motion of thousands of kilograms of food crops through silos or conveyor belts is being studied, while in the case of inhalers, only a few grams of powder are being transported.

The Kastrup lab from UBC developed a series of hemostatic powders for non-compressible intra-abdominal hemorrhage (NCIAH) [36]. In their work, they tested their product on living animal tissue and reported that the powder could extend the survival of living organisms that

were severely injured or thermodynamically unstable by several hours. After the successful development of a hemostatic powder for NCIAH, the Kastrup Lab developed a hemostatic powder for UGIB cases. The difference between NCIAH and UGIB is the environmental conditions within the body. In the former case, during a surgical procedure, the surrounding environment consists of blood, while in the latter case, the environment consists of air.

Even though the specific content of the UGIB powder was not revealed to our group for this specific project, a general behavioral characterization of the powder was provided. The main parameter with a high influence on powder flowability is the adhesive behavior of its particles. This adhesive characteristic often leads to blockage within the catheter due to caking.

"Hemospray", a device manufactured by Cook Medical for the delivery of medicinal powder through a catheter, was tested by the Kastrup lab team. They concluded that the device is not operating efficiently with the hemostatic powder due to the aforementioned adhesive properties of the powder.

The next spraying device tested on pigs by the Kastrup team consisted of a high-pressure canister of CO_2 connected to a chamber filled with powder. The chamber was connected to a catheter through a Venturi tube, so the powder was deposited on the stomach walls. During the tests performed by surgeons, it was observed that the powder was sprayed everywhere, causing reduced visibility inside the stomach, which can be dangerous during the surgery. Figure 1 shows how UGIB is formed in the stomach walls. This image was taken during in-vivo experiments that were performed on pig stomachs at the initial stages of this research using the device described previously. The white part of the image is the catheter that was used during the experiments.

Figure 1: **Direct image from a surgical monitor during in vivo experiments that were performed on pig stomachs diagnosed with upper gastrointestinal bleeding.**

The device was found to be lacking in performance as the flow would stop frequently. These underperforming devices indicated the need to create a robust medical device and showed the important tasks that this project needs to achieve.

The main tasks of the current project can be summarized as follows, based on the requirements that need to be met:

- Design a device to deliver the adhesive hemostatic powder through a catheter of 0.002 m in diameter and 1.47 m in length into the stomach interior.
- Deposit the powder with high accuracy while avoiding a possible blockage of flow.

- Deliver 5-7 gr of powder within a short period of time (10 to 30 s).
- Limit the pressure output based on the stomach's tissue tolerance to pressure.

The time limitation, provided by the Kastrup Lab team, is based on stomach expansion tolerance. By reducing the delivery time of the hemostatic powder, we reduce the volume of gas inserted into the stomach. It must be noted that there is no immediate danger if the stomach reaches its volumetric capacity since the doctors can remove any unnecessary gas using the endoscope.

It must be noted that the hemostatic powder is still under development, so we were unable to characterize its properties properly. Therefore, we used lactose to obtain the initial results, which will be used as a reference for future tests. The reason behind this choice will be explained in Chapter 4.

Regarding the powder blockage due to the agglomeration and caking of the solid particles, during the current research, it was found that a continuous flow minimizes the chances of blockage while increasing control over the particle mass flow rate and deposition.

To satisfy the requirements, an experimental setup has been built, and computational studies have been performed. In this research, we examine how various initial conditions, such as the gas flow rate and the powder mass flow rate, affect the pressure drop over the length of the catheter. A recently developed method of 4-way coupling between Computational Fluid Dynamics (CFD) and Discrete Element Method (DEM) was used to calculate the flow regime numerically. This method is suitable for solving high-velocity turbulent dense multiphase flows, while it helps reduce the computational cost and accurately calculate interparticle forces [20]. The results of the simulations are compared to the experimental results. To our knowledge, there is no academic research related to the characterization of turbulent, dense granular flows at such a small and high gas velocity inlet.

1.2 Objective

The general objective of this work is the development of a novel device for hemostatic powder delivery to treat gastrointestinal bleeding. The specific objectives of this project are as follows:

1. Design optimization of the device prototype for the treatment of UGIB.
2. Model development for turbulent and dense granular flows through a catheter using CFD-DEM coupling and result verification.

1.3 Organization

Chapter 2 provides background information on different approximation methods for granular flows, their role and application in the industry, as well as previous work done for the characterization of dense granular flows. Furthermore, a more detailed analysis is presented, along with a brief background on the current epidemiological work and a thorough view of the current treatment methods for UGIB.

Chapter 3 presents the experimental setup along with a description of each component that defines it. Additionally, the limitations and the factors that influenced the design will be discussed.

In Chapter 4, the numerical approach is analyzed. Following the detailed introduction on CFD-DEM coupling, an analytical discussion on force balance and the governing equations is made. Finally, a more insightful view of the CFD-DEM coupling is given, along with the material properties that define the simulations.

Chapter 5 is dedicated to the results from both simulations and experiments. After presenting the findings of each case, a comparison between the two will follow.

In Chapter 6, the overall conclusions of this thesis, future work, contribution, and limitations are discussed.

Chapter 2: Background

The current research has a multidimensional aspect rather than a purely mechanical or medical one. Thus, it was decided that this chapter should be divided into three parts. The first part offers an insight into multiphase flows. The second part addresses the engineering aspect of the project by analyzing the previous work regarding the numerical approximation of dense granular flows. In addition, details regarding the differences between various numerical models as well as an insight into previous work in the field on computational approximations are presented. The last part consists of a detailed analysis of upper gastrointestinal bleeding as well as background work and treatment analysis. Finally, a discussion on medical restrictions will follow.

2.1 Multiphase flows

Before moving forward with the mathematical models that describe problems like the current one, it is essential to present the physical interpretation of multiphase flows. The term multiphase flow refers to flows that consist of more than one phase of matter. For example, there are gas-solid, liquid-solid, and liquid-gas flows. These types of flows are very common in the industry but very complex. Some examples involve bubbly flows in nuclear reactors, fluidized beds in the food industry, petroleum extraction, and drilling where solid ground is mixed with oil to create a two-phase fluid.

The complexity of these flows originates from the type of each phase, particle interactions, the velocity of the transporting medium, and the phase concentration of each matter in the mixture, called the volume fraction. Throughout the years, a lot of studies have been dedicated to

categorizing multiphase flows based on these parameters, some of which are slurry flows, aerosols, fluidized beds, and others. The reason behind the study of these flows is the need to understand them in depth to improve their performance for different applications. For the case of nuclear reactors, a detailed analysis can be found in the book of Bahman Zohuri [37], while a study on multiphase flows in gas and oil applications can be found in the work of Baojiang Sun [38].

In the current study, we focus on gas-solid multiphase flows. Another term that can be associated with gas-solid flows is granular flow. As mentioned earlier, two important factors that define multiphase flows are the volume fraction of each phase and the velocity of the transporting medium. The impact of these parameters on the flow regime and their behavioral patterns can be found in detail in Lian-Shih Fan's and Chao Zhu's book [39]. In their work, they analyze, describe, and characterize gas-solid multiphase flows. A more detailed background on granular flows is presented in the following section.

2.2 Dense Granular Models

Over the years, several models have been introduced to replicate and accurately calculate granular flows. Since the application of each model is not robust, meaning that different models will behave better in specific scenarios, examples of applications in the industry will be introduced alongside the advantages and disadvantages of each model.

2.2.1 Two-Fluid Flow

The first model that is introduced is the Eulerian-Eulerian two-fluid model (TFM). Ding and Gidaspow [21] developed TFM to help with the quantitative understanding of the hydrodynamics of complicated fluidized beds. The TFM approach treats both solid particles and fluid particles as continuous phases. To approximate a solution, the fluid domain is divided into smaller domains, creating a mesh. Since one phase cannot contain another, volume fractions are being introduced. For the model to converge, conservation equations of mass, momentum, and energy are solved for each phase. After considering the constitutive relations for the solid phase, the solution is then achieved using the kinetic theory of granular flow [25] [26]. Examples of industrial applications of TSM can be found in the work of Nikolopoulos et al. [24]. In their work, they test the accuracy of TFM with experimental data on circulating fluidized beds. They concluded that the simulation results predicted the experimental ones with an accuracy of less than 2%. Xi-Zhong Chen et al. [22] used the TFM to replicate the gas-solid fluidized bed of polymerization reactors using a 2D CFD model. The model was verified by comparing pressure drop and velocity data with already-existing mathematical models. Nan Zhang et al. [23] use the TFM model while considering the size, the size distribution, and the velocity of the particles, but a detailed analysis of particle interaction with other particles or the boundary is not considered.

2.2.2 Dense Discrete Phase Model

The dense discrete phase model (DDPM) is a formulation of the Eulerian-Lagrangian multiphase flow. While the fluid is treated as a continuous phase, the solid particles are tracked individually. Muhammad Adnan et al. [30] compare the numerical performance of TFM and DDPM in a bubbling bed reactor. After conducting 2D simulations for the two models, they reported that the DDPM model prevailed over the TSM one. The key factor behind this conclusion was grid independence. As reported, the DDPM retained complete grid-independence on both fine and coarse grids, while the TSM did not. This led to a much faster computational speed; more specifically, the DDPM case concluded the computational process six hours before the TSM. Even though particle tracking and grid independence are great assets for the DDPM, there are some limitations associated with this model. As reported in [25] and [29], the model is limited to flows close to the packing regime, meaning that it cannot be used when large-scale systems are simulated. The next model was created to overcome such limitations.

2.2.3 Discrete Element Model

The next method is the discrete element method (DEM). The advantage of this method in relation to the TSM is the detailed consideration of particle interaction with other particles and boundaries. Additionally, the DEM is characterized by a lack of mesh implementation, which is needed for both DDPM and TSM. Since the equation of motion is solved for each particle according to Newton's laws, there is no need to solve the stress-strain constitutive law for the material. Each force responsible for motion, such as body forces, particle-particle forces, and

particle-boundary forces, is calculated individually for each particle over time [28]. Moreover, the DEM approach offers the advantage of incorporating particle morphology such as size and density into the solution, offering a more realistic solution for dense granular flows [27]. A great example of DEM usage is the study of fluidized beds. M. Xu et al. [29] successfully replicated the experimental process of a fluidized bed in a computational environment using DEM modeling. For the 3D simulation scenario, the comparison between simulation and experiments was conducted by observing the particle patterns, and the results were satisfying. The main disadvantage of DEM, as stated in [29], is the demanding computational cost, which increases as the number of particles increases. In their work, a CPU (Central Processing Unit)-GPU (Graphics Processing Unit) hybrid computational mode was used to divide the workload. The CPU is responsible for the fluid flow computation, while the GPU focuses on particle motion.

2.2.4 CFD-DEM System Coupling

To overcome the high computational cost while broadening the applications where the DEM method can be applied, a new method using CFD-DEM coupling has been developed. This new approach follows the Eulerian-Lagrangian approach, where the fluid is treated as continuous while particle interactions are individually tracked [26]. The difference between this model and the DDPM one lies in model execution. In a CFD-DEM system, both models are solved simultaneously. Once the system initiates, the CFD model captures the behavior of the fluid, while the DEM focuses on particle forces and interactions. During the solving process, an exchange of data takes place between the two solvers to update and calculate the flow regime

accurately. Since the DEM solver can be executed using the GPU and the CFD part is run through the system's CPU, it is possible to execute demanding simulations [31].

Due to the complexity of this research, which is focused on high-velocity dense granular flows in confined spaces, a CFD-DEM approach is followed. For this specific task, Ansys Fluent and Rocky DEM are used. Fluent and Rocky are both tools provided by Ansys. More details on the system coupling and models used will be presented in Chapter 4.

2.3 Medical Perspective

This section is dedicated to the medical aspect of this research. The case of the UGIB will be examined, starting with a brief introduction, which will be followed by the background of this medical condition, the current ways of treatment, and finally the restrictions applied to this project.

2.3.1 Upper Gastrointestinal Bleeding

UGIB refers to the internal bleeding within the stomach area. As previously mentioned in the introduction, UGIB, is a medical condition that affects 67-102 per 100,000 people [8] [9]. These statistics were conducted in the USA during the last two decades of the 20th century and the first two decades of the 21st century. Furthermore, these statistical data represent the cases of people who were hospitalized. Even though the cases of hospitalization seemed to be decreasing over time, the mortality rate did not change [9], which shows the importance of understanding the UGIB in depth as well as the ineffectiveness of the current treatment methods.

2.3.2 Background

Anatomically, gastrointestinal bleeding refers to internal bleeding caused in the section between the stomach and anus. Since this condition covers a large area of the human body, it has been divided into two sections: UGIB and lower gastrointestinal bleeding (LGIB). The UGIB refers to the bleeding at the esophagus, stomach, and duodenum (the first section of the small intestine), while the LGIB refers to the bleeding at the jejunum, the ileum, the large intestine, the rectum, and the anus. There is one more reason behind this separation, and that is the differences in etiologies, as mentioned by Chad T. Whelam et al. [1]. One of the examples mentioned in their work states that acid-related diseases are usually responsible for causing UGIB without affecting the areas in which LGIB occurs. In this project, only the UGIB case will be covered, with the stomach being the primary focus.

According to M.E. van Leerman [2], the main causes of UGIB are peptic ulcer bleeding, the most common case, and various erosive diseases. Finally, thorough research on different etiologies characterizing upper gastrointestinal bleeding can be found in the work of Amrit K. Kamboj et al. [3], where they discuss the impact of gastric varices, gastric malignancy, and dieulafoy lesions in human health.

It must be noted that every author mentioned previously emphasizes that hemorrhage is commonly characterized by its intensity. There are several stages, with acute bleeding being the most severe one. Cases characterized by this category could lead to life-threatening conditions and must be dealt with immediately. This shows the importance of the introduction of various

treatment methods, which should then be compared to find the safest and most robust method that can potentially save the most lives.

2.3.3 Treatment Analysis

In this section, the different treatment methods will be presented for non-variceal UGIB bleeding. In their work, Luis Lau and Joseph Sung [4] have analyzed the four current techniques used for treating UGIB. The first technique is standard endoscopic therapy (SET). The SET treatment consists of three different methods that approach this medical issue in a different manner. The first one is an injection of diluted epinephrine to slow down the bleeding. This solution can only provide temporary effects since there is a high chance of rebleeding. The second one is thermal therapy. High temperatures or electrical currents produced by thermal coagulation devices can cause the activation of the coagulation cascade and tissue edema. The risks of this method are potential thermal injury and an increased risk of delayed bleeding. The third one is the use of a through-the-scope clip.

This technique focuses on hemostatic powders. In their work, J.J.Y. Sung et al. [5] studied the effectiveness of hemostatic powder treatment in 20 patients. In their study, they report that they managed to reduce bleeding by 95% in 19 out of 20 patients. An extensive study on different products of hemostatic powder is presented in [11]. Even though the test sample might not be sufficient to generalize the efficiency of hemostatic powder, it provides a great insight into how useful it can be, given the low risk of surgery complications.

2.3.4 Gastrointestinal Restrictions

To create a first prototype, at least for the experiments, which would act as a steppingstone for the design optimization of the actual device prototype, various parameters of medical nature need to be considered. The first one is derived from the experience gained through in vivo experiments on pigs. These tests took place during the current research with the sole purpose of testing the effectiveness of the powder on real surgical conditions. During those experiments, an approximation of the optimal total deposited mass of powder on the area affected by UGIB was determined, as well as the duration of the delivery. The second parameter, which is the most important, is focused on the patient's safety. A primary concern during the design was to ensure that no further injuries occurred, causing the UGIB to worsen. Since clinical trials were not performed, the experimental protocol does not have to obey the sanitary rules of a surgical room; thus, the restriction discussion will initiate with organ integrity.

For soft tissue tolerance, two research papers were taken into consideration. The first one is a study by G.F.B.A. Kaehler et al. [6]. In their work, they use a 70-bar water jet dissector for mucosa elevation. They conducted an in-vivo trial with eight pigs using adult pig stomachs. The purpose of the experiment was to form water cushions for mucosal elevation. They reported that the ideal running time for these experiments was 10 s. They conclude that if the pressure was set in the range of 50 to 70 bar, the water jet would be able to penetrate the gastric mucosa successfully while creating the ideal elevation. When the pressure was set to 30 bar, they could not create any utilizable water cushion, and once the pressure was over 100 bar, injuries would occur.

While this research paper gives an estimation of stomach tissue tolerance, their application was different from the current work since they needed to find the optimal pressure range to properly injure the stomach.

This leads to the next work done by Teruo Hoshino et al. [7]. Their work is similar to the current project and offers a great insight into how the suspension of solid particles in air behaves in the stomach. For their experiment, they used seven mongrel dogs weighing around 10 kg. The setup consisted of an air gun adapted to work with an endoscope loaded with a cartridge filled with powder. They run experiments with various substances such as NaCl, KCl, aspirin, and others. The results showed that a pressure of 2 kgf/cm^2 (28.4 psi, 1.96 bar), measured at the outlet of the catheter, is the threshold right before any damage is caused to the organ tissue.

The pressure magnitudes in the two references differ by two orders of magnitude. The data presented in [7] were considered more relevant for the present research, so the pressure of 28.4 psi is the maximum allowable outlet pressure.

Finally, it should be mentioned that this pressure limit was mentioned to the surgeons doing the animal testing. They verified that it was a safe pressure for the stomach tissue.

2.4 Conclusions

In this chapter, the background work was presented. The analysis started with the description of multiphase flows. The discussion proceeded with a detailed comparison between the existing computational models for granular flows. Several models were mentioned, such as the TSM and DDPM. It was concluded that the ideal approach for our case was the CFD-DEM coupling system. The second part of the background work was focused on the medical aspect of the

project. A detailed definition of UGIB was presented, as were the current treatment methods. In the final part of this chapter, some of the essential restrictions that defined this project were mentioned.

Chapter 3: Experimental Setup

3.1 Introduction

Designing and building the experimental device was one of the most important steps that defined the outcome of this project. There are many parameters that need to be considered, from cost to a simple design that can easily be handled by a doctor during surgery. Since the project was in its initial stages, the current device was built to work in a laboratory and not in the operating room (OR). This means that some changes in the design will be implemented as the project moves forward to address all the risks and health regulations needed for the OR.

A general image of the setup is provided in Figure 2. The area marked “1” indicates the sensor for measuring the pressure drop as well as the flow rate regulator. The area marked “2” is the main body of the device, the Active Cyclone, and its connections to the compressed air gas line. The area marked “3” corresponds to the electronic setup and the Arduino, and finally, the “4” mark shows the catheter connection to the container, which was used to deposit the powder.

In the following sections, design limitations will be discussed, along with a thorough discussion of each part. Finally, in Appendices A and B, the improvement of the cyclone geometry is discussed, along with the cost analysis of the device prototype.

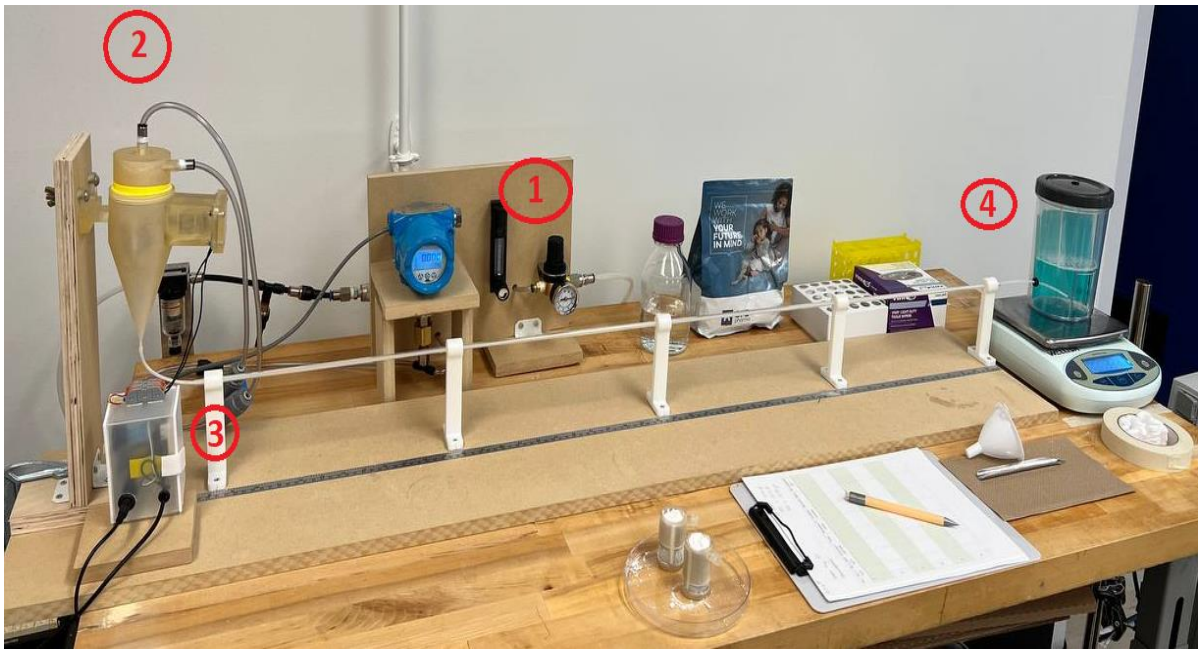

Figure 2: Experimental setup 1) Sensor 2) "Active Cyclone" 3) Arduino 4) Catheter and container.

3.2 Setup Components

The device prototype was designed to be simple and effective while keeping its production at low cost. This approach allowed constant improvement while helping with the simplification of the setup.

3.2.1 Sensor

For the experiment, a single pressure sensor (model: Tek-Bar 3120B, make: Tektrol) was used to capture the pressure drop. The specific sensor is a gauge type of pressure sensor with an accuracy of ± 0.075%. For the calibration processes, the zero value was set, and then the sensor was connected to an Arduino Mega, which captures the pressure changes every 1 second. The

sampling frequency of 1 Hz was selected based on the response time on the sensor's diaphragm, which is ≤0.2 s, meaning that a selection of a higher frequency could produce unreliable results. Since the initial conditions strongly influenced the experimental results, we determined the gas flow rate first. The values of the gas flow rate were set using a flow regulator.

3.2.2 Active Cyclone Working Principle

A solenoid was placed within the main body of the cyclone, as can be seen in Figure 3. The motion of the solenoid is controlled by a second Arduino. On its shaft, a sieve created by a 40 by 40 (40 grids per inch) mesh is placed. The sieve was used to break down the powder agglomerates; therefore, the powder mass flow rate is more uniform.

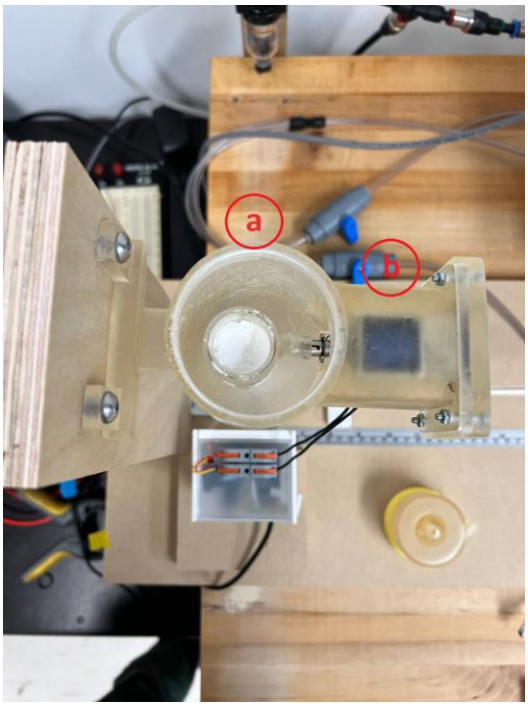

Figure 3: Sieve-chamber (a) and solenoid (b) placement within the cyclone.

During the experiments, three sieve chambers with the same mesh and different active heights were used to test how different powder mass flow rates affect the pressure drop.

As the sieve was placed into the cyclone, the cyclone lid was closed tightly to seal any potential gas leakage that could impact the measurements. After that, the device was turned on and the solenoid started moving the sieve back and forth with a frequency of 10 Hz until all the powder was emptied from the chamber.

In Figure 4, three different sieves can be seen. The one on the left (a) has the largest active surface, while the one on the right (c) has the smallest. The selection of the best chamber was made based on the number of blockages in the flow.

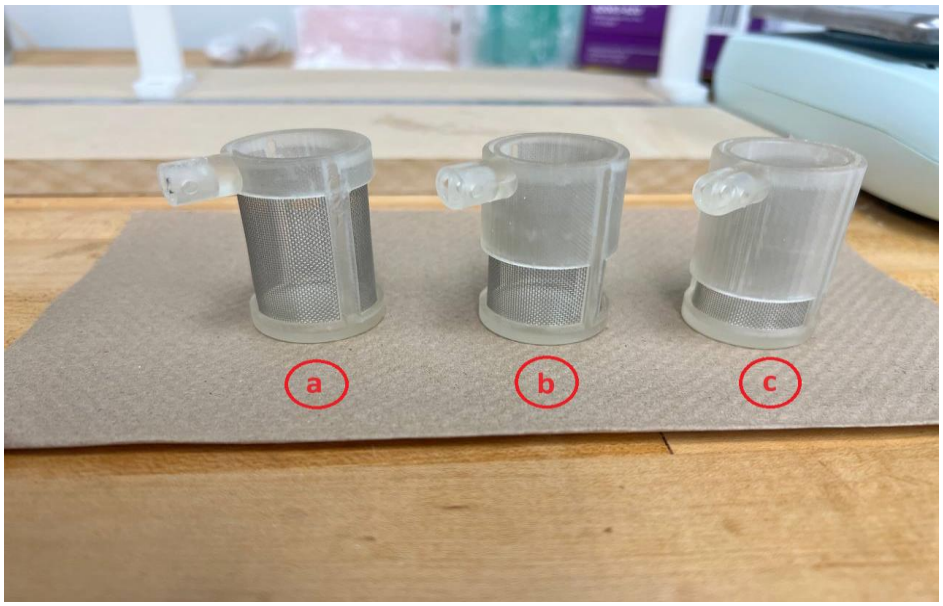

Figure 4: Three different sieve designs based on the active surface of the mesh a) No coverage b) 50% coverage c) 75% coverage.

Table 1: The effects of the frequency and chamber type on the number of blockages in the flow.

Camber	No of Trials	Frequency (Hz)	No of Blockages
a	5	10	5
b	5	10	3
c	5	10	0
a	5	20	5
b	5	20	5
c	5	20	3

In Table 1, the performance of the different chambers based on the number of blockages per trial is presented. Any chamber that shows blockage cannot be selected for the final design. One set of tests was successful: the chamber “c” at 10 Hz.

3.3 Design Limitations and Influence Factors

Some of the limitations that derive from the medical restrictions were mentioned in Chapter 2, but in this section, all the factors that affect and restrict the design will be discussed.

The most important factors that defined the design are the tissue tolerance to pressure and the feedback, regarding the conditions and the behavior of the hemostatic powder, received from the Kastrup Lab team and surgeons during in-vivo experiments at the early stages of this project.

To respect the soft tissue tolerance to pressure reported in a previous study [7], the inlet system pressure was set to 10 psi (68.9 kPa), which was 19 psi (131.8 kPa) lower than the maximum pressure limit for tissue failure. Since the system introduces losses, the pressure was expected to drop even further, leading to a pressure outlet lower than 5 psi. The system pressure drop as measured from the experiments is reported in Chapter 5. The total mass of the powder needed, as well as the powder delivery time, were communicated to us by the Kastrup team. It was shown that after depositing a minimum of 5 g of powder onto the affected area, any hemorrhage would stop within 30-60 s. To keep up with the performance standards, a sieve with a capacity of 10 g was developed, while the system can deliver approximately 95% (Chapter 5) of the total mass continuously within 15-30 s, depending on the gas flow rate.

Ideally, to study the powder behavior inside the cyclone and test how effectively the dense granular mix of gas and powder is transferred into the catheter, a series of simulations would be required. Unfortunately, this was not possible, given the computational capabilities of the computers used. To overcome this obstacle, it was decided to approach this issue from a different angle, using an experimental method. The powder flowability was examined based on the different inclination angles of the cyclone. The success of each design was decided based on the times that blockage occurred during the trials, the total mass of powder that was deposited in the container, and the delivery time. More details regarding the selection of the most efficient design will be given in Chapter 5.

Furthermore, during the experiments, lactose powder was used instead of hemostatic powder. It was mentioned earlier that the development of the hemostatic powder is still in progress, making the proper evaluation of its properties impossible. The selection of lactose was based on its adhesive properties. Both lactose and the hemostatic powder developed by the Kastrup Lab team

are defined by similar adhesive behavior, making lactose the best option for our experimental studies.

It must be mentioned that during the experiments conducted in this project, lactose of 70± 30 μm was used, with the majority (~90%) of the particles being 70 μm (manufacturers: Alphachem, DFEpharma). The list of lactose properties will be presented in Chapter 4.

3.4 Conclusions

The prototype of a device was built to efficiently deliver adhesive medicinal powders through a catheter. The prototype was 3D printed and was designed to efficiently deliver hemostatic powder while respecting medical restrictions. An experimental setup has been built to measure high-velocity, dense granular flows in a laboratory while respecting the optimal conditions in which the hemostatic powder can operate.

Chapter 4: Numerical and Modeling Approach

This chapter is dedicated to the mathematical description of the governing equations and boundary conditions that define the flow of air and solid particles through the catheter and the numerical setup for this problem.

The chapter is divided into three main parts. The first one is a brief discussion regarding particle behavior, forces that take place in the specific experiment, the interaction between fluid and solid particles, followed by an explanation of the force interaction between fluid particles and solid particles and an interaction between the CFD and DEM models. The second part will give a detailed analysis of the governing equations that define the problem. The final part of this chapter is dedicated to the numerical setup of the simulation. As will be thoroughly discussed later, the DEM is responsible for particle behavior, specifically tracking and particle forces. These parameters are then translated into velocity and momentum information for CFD. It must be mentioned that the parameters are strictly related to the characteristic properties of the powder, such as particle size and morphology, as well as the force models that define the system.

4.1 Introduction

The first step is defining the granular flow type that characterizes the problem [20]. The main parameter that categorizes the working flow regime in this experiment is the volume fraction of the solid particles. This variable is, basically, an indication of how particles act in the fluid flow. For a solid volume fraction of $\alpha_i \leq 10^{-6}$ it can be safely assumed that the particles do not affect

the flow, and in this case, a CFD-DEM approach is not suitable since the particle behavior can be neglected. For a solid volume fraction of $10^{-3} \leq \alpha_i$, which is the case this project is examining, the volume of particles in the fluid is enough to affect the behavior of the flow.

To properly describe how such a complicated system works, it is essential to discuss the CFD and DEM models, followed by a detailed description of how these models interact [20] [32].

The CFD-DEM approach is based on the Eulerian-Lagrangian model. The CFD part is approached with the Eulerian model, which treats the fluid as a continuous phase. The mathematical modeling of the fluid is done using the Reynolds-averaged Navier-Stokes equations. The DEM part, as mentioned before, only includes solid particle behavior, from tracking to force analysis. This makes it essential to observe each particle individually. Hence, the Lagrangian approach was chosen. Since DEM needs to provide CFD with the forces acting on each particle, the discrete element method is characterized by the governing equations of Newton's second law of motion.

The CFD-DEM was chosen over other models, such as the Discrete Phase Model and Dense Discrete Phase Model Incorporated with the Kinetic Theory of Granular flow (DDPM-KTGF), due to its advantages. The main one is the realistic approach to particle interaction during collisions. Unlike other models, CFD-DEM gives the opportunity to use models to simulate the adhesive behavior of particles, even non-spherical ones, to provide a more realistic approach while keeping the computational cost relatively low [33].

It is essential, at this point, to explain how the CFD-DEM coupling works. In a CFD-DEM coupling formulation, the CFD part solves the governing equations for the fluid flow and provides the necessary force information to the DEM to calculate the forces that act on the solid

particles. Once this information is delivered, the DEM calculates the new position and velocity for these particles and sends it back to the CFD.

To choose the proper approach for the current research, the review work done by Mahmoud A. El-Eman et al. [20] was taken into consideration. As mentioned in their work, the most crucial parameter that determines the coupling method is the solid particle volume fraction α_i. If its value is small enough ($\alpha_i \leq 10^{-6}$), then the system can be defined with one-way coupling. This method is used when the solid particles have a very small effect on the flow. Thus, the particle motion and behavior within the fluid are fully defined by the fluid itself.

When the solid volume fraction increases ($10^{-6} \leq \alpha_i \leq 10^{-3}$), the interactions between fluid and solid particles cannot be neglected anymore. The implementation of particle influence has become essential, and a CFD-DEM system will define the simulations. As mentioned before, the CFD translates the forces obtained by the DEM into particle velocity. Once the CFD system is updated, the new state of the particles is transferred to the DEM once more to repeat the calculation. This method is called two-way coupling. The final coupling method, named four-way coupling, acts in a similar manner as the previous one, but since the solid volume fraction is increased even further ($10^{-3} \leq \alpha_i$), the flow becomes denser; thus, the accurate prediction of particle behavior becomes essential for an accurate flow prediction. In this method, particle-flow-particle, particle-boundary, and particle-particle interactions are taken into consideration. All these interactions make it clear that each model needs to be carefully chosen for each problem; thus, the following few sections will be devoted to forces involved in a CDF-DEM four-way coupling system.

4.2 Particle Phase Modeling

It is important that we mention the assumptions made for solving the problem. The first one is that the problem is considered isothermal. This assumption was made due to the nature of the project. As mentioned in a previous section, the goal of this research is to create a device that is capable of delivering a hemostatic powder to the interior of a human stomach. Since the temperature difference between the environment and the patient is not considerable, it was chosen to neglect its effects.

The second assumption is that the particles are spherical. Even for the experiments, as will be seen in Chapter 5, the powder was chosen to have particles that were close to spherical. The third one is that the rotational effects on the particles have been neglected. It was assumed that the energy consumed by a possible rotation of the particles is not considerable. Thus, it would not affect the outcome of the problem in any way. Finally, it must be noted that the assumptions regarding the fluid will be reported in the fluid flow modeling section.

As has already been mentioned for solid particles, the Lagrangian approach is required. The DEM solver keeps track of each particle's state, and to do that, the explicit solution of Euler's first and second laws is required. Thus, the particle-governing equations for the DEM solver are given by the following relation:

$$m_p \frac{dv_p}{dt} = F_c + F_{f \to p} + m_p g \qquad (1)$$

F_c represents the contact forces. These forces involve particle-particle and particle-boundary interactions. g refers to the gravitational acceleration while m_p refers to the mass of solid particles. Finally, $F_{f\to p}$ represents the fluid interactions with the solid particles. More details regarding these forces will be given in a later section.

4.2.1 Normal Forces

Even though there are several models available for describing normal forces, in this work the hysteric linear spring model developed by Walton & Braun was chosen [28]. The main reasons behind this decision are based on the low computational cost and high accuracy of simulating compressible materials.

The expression that defines normal contact forces is the following:

$$F_n^t = \begin{cases} \min\left(K_{nl}s_{n,}^t \;\; F_n^{t-\Delta t} + K_{nu}\Delta s_n\right), & if\ \Delta s_n \geq 0 \\ \min\left(F_n^{t-\Delta t} + K_{nu}\Delta s_{n,} \;\; \lambda K_{nu}s_n^t\right), & if\ \Delta s_n < 0 \end{cases} \qquad (2)$$

Where:

$$\Delta s_n = s_n^t - s_n^{t-\Delta t} \qquad (3)$$

In the first relationF_n^t, $F_n^{t-\Delta t}$ express the contact forces at the current (t) and previous timestep (t-Δt). Similarly, the values $s_n^t, s_n^{t-\Delta t}$ represent the values of normal overlap during two successive time steps, while their difference represents the change in the contact overlap in the current time

step (Figure 5). The parameter λ is a dimensionless constant that is used to cancel the normal forces when the particles don't overlap anymore. Its value is set at 0.001 in Ansys Rocky.

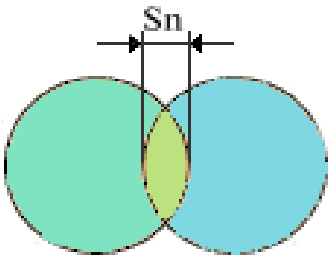

Figure 5: Overlap of two solid particles.

It must be mentioned that the contact between particles is considered plastic deformation. Once the particles detach, any plastic deformation is "forgotten", and the particles return to their original shape. The energy that was dissipated during the collision is numerically equal to the green area formed by the two particles in Figure 5. K_{nl} and K_{nu} describe the loading and unloading stiffness of the particles during a collision. These terms are calculated based on the coefficient of restitution, ε, which represents the energy dissipation during the collision of particles. This parameter depends on the material. In this study, we use lactose, its material properties will be given later in this chapter.

In the following equation, there are two loading stiffness parameters. The first parameter is used to describe particle-particle interactions, while the latter one is used for particle-boundary interactions.

$$K_{nl,p} = E_p\, L \qquad (4.1)$$

$$K_{nl,b} = E_b\, L \qquad (4.2)$$

E_p and E_b are the Young's moduli for the particle and the boundary, respectively. For E_p we consider the bulk modulus and L is the particle size. Since in this work the particles are considered to be spherical, L represents the particle's diameter. $K_{nl,p}$ and $K_{nl,b}$ represent the loading stiffness of particles and boundaries respectively.

The unloading stiffness is defined by the energy dissipation during the contact due to the plastic deformation.

$$K_{nu} = \frac{K_{nl}}{\varepsilon^2} \qquad (4)$$

4.2.2 Tangential Forces

After choosing the normal forces, it is important to define the tangential forces. The best model for this specific problem was determined to be the Coulomb limit model, which is given by the following expression [28].

$$F_\tau = -\mu F_n \frac{\dot{s}_\tau}{|\dot{s}_\tau|} \qquad (5)$$

In this equation F_n is the normal force during contact, $\dot{s}_\tau$ is the tangential relative velocity vector, and μ is the friction coefficient, which is given by:

$$\mu = \begin{cases} \mu_s, when\ particles\ do\ not\ slide \\ \mu_d\ , when\ particles\ slide \end{cases} \qquad (6)$$

μ_s is the static friction coefficient and μ_d the dynamic one. If the relative velocity between two particles is lower than 0.001 m/s, there will be no sliding.

4.2.3 Adhesion Forces

The main property that defines the particles from the hemostatic powder during the flow is their adhesive nature. Since this powder is a new product that is not yet characterized, it was decided to explore the particle behavior using a well-known material with some similarities to the hemostatic powder. The material that was chosen for this project was lactose. Lactose particles have a similar adhesive behavior to hemostatic powder. Lactose's properties are well characterized, making them easier to study. Using lactose, we aim to create a benchmark for future studies on hemostatic powders. To model the behavior of these particles, it is essential to introduce the equation that describes adhesion [28].

$$F_{n,adh} = \begin{cases} 0\ , & if\ -s_n \geq \delta_{adh} \\ r_{adh} K_{nl}(s_n + \delta_{adh}), & otherwise \end{cases} \qquad (7)$$

$F_{n,adh}$ is the adhesive contact force for the running time step and, δ_{adh} is the "adhesive distance". If the adhesive distance is larger than the separation distance, s_n, the adhesion force will be zero. As already mentioned, s_n is the contact overlapping distance between two particles

or between a particle and a wall. s_n is positive when two objects touch each other and negative when they are close to each other but there is no contact. r_{adh} is the ratio of adhesive stiffness to contact loading stiffness and K_{nl} is the loading contact normal stiffness, which is defined by the following expression:

$$\frac{1}{K_{nl}} = \begin{cases} \frac{1}{K_{nl,p1}} + \frac{1}{K_{nl,p1}}, for\ particle - particle\ contact \\ \frac{1}{K_{nl,p}} + \frac{1}{K_{nl,b}}, for\ particle - boundary\ contact \end{cases} \quad (8)$$

4.2.4 Drag Forces

Different drag models from the DEM software can be selected for either dense or non-dense flows. The solid volume fraction in this problem was found to be $\alpha_i = 3.23 \cdot 10^{-2} \geq 10^{-3}$, thus the model of Huilin and Gidaspow can be selected due to its robustness. This model can work for the entire range of solid volume fractions. This robustness derives from adapting two different models into one. The first one is the model by Ergun, and the second one is by Wen and Yu [32]. The coefficient of drag is given by:

$$C_D = \psi C_{D_E} + (1 - \psi) C_{D_W} \quad (9)$$

The variable ψ is the blending parameter and is given by the following expression as a function of the fluid fraction a_f.

$$\psi = \frac{\arctan\left(262.5(0.8 - a_f)\right)}{\pi} + 0.5 \qquad (10)$$

C_{D_E} is the Ergun drag coefficient given by:

$$C_{D_E} = \frac{200\alpha_s}{\alpha_f \varphi^2 Re} + \frac{7}{3\varphi} \qquad (11)$$

where α_s and α_f are the solid and gas particle volume fractions, respectively, Re is the Reynolds number of the gas, and φ represents the particle sphericity, which is calculated by:

$$\varphi = \frac{A_{sph}}{A_p} \qquad (12)$$

A_{sph} and A_p represent the surface area of a sphere of the same volume as the particle and the actual surface of the particle, respectively.

C_{D_W} represents the drag coefficient given by Wen and Yu [32] and it is given by the following expression:

$$C_{D_W} = a_f^{-1.65} \max\left\{\frac{24}{a_f Re_p}\left[1 + 0.15\left(a_f Re_p\right)^{0.687}\right], 0{,}44\right\} \qquad (13)$$

where Re_p is the Reynolds number calculated with respect to the particle diameter.

4.2.5 Pressure Gradient

The flow of air and solid particles is driven by the pressure gradient. It is important to analyze how the pressure affects particle motion [32].

$$F_{\nabla p} = -V_p \nabla p \qquad (14)$$

Where $F_{\nabla p}$is the force due to the pressure gradient, ∇p. Lastly, V_p is the particle volume.

4.3 Fluid Flow Modeling

The two main parameters defining the flow regime are the powder and fluid flow rate. Both parameters were defined experimentally. The details of this process will be thoroughly explained in Chapter 5.

It was found that the Reynolds number for the air at the entrance of the device is higher than the critical Reynolds number; hence a turbulent model has been used for simulations.

The model chosen for this project was k-ω SST. The reason behind this choice lies in the capabilities of this model over k-ε and k-ω. K-ω SST provides a great tool for predicting and calculating eddy formation while providing accurate flow behavior near the boundaries [25]. As mentioned previously, the particle-boundary interaction is taken into consideration in this problem due to the adhesive properties of the powder. This adhesive behavior is partially responsible for the deposition of particles on the wall, which makes k-ω SST the best model for this problem.

Since the forces on particles have been analyzed, it is now essential to present how these forces are implemented into the CFD equations. The CFD model is solved using the Reynolds averaged mass and momentum conservation equations. The averaged momentum conservation equation can be found by [32]:

$$\frac{\partial}{\partial t}\left(a_f \rho_f \boldsymbol{u}\right) + \nabla \cdot \left(a_f \rho_f \boldsymbol{u}\boldsymbol{u}\right) = -a_f \nabla \mathrm{p} + \nabla \cdot \left(a_f \mathbb{T}_f\right) + a_f \rho_f \boldsymbol{g} + F_{p-f} \qquad (15)$$

where ρ_f is the fluid density and *u* is the fluid velocity. The averaged mass conservation equation is given by:

$$\frac{\partial}{\partial t}\left(a_f \rho_f\right) + \nabla \cdot \left(a_f \rho_f \boldsymbol{u}\right) = 0 \qquad (16)$$

In the previous equations, *f* represents the fluid and *p* represents the particle. The two terms that have not been analyzed yet are the stress tensor and the force that represents the interaction between the two phases $F_{p\text{-}f}$.

The fluid viscous stress tensor, $\mathbb{T}_f$, is calculated:

$$\mathbb{T}_f = \mu_f(\nabla \mathrm{u} + \nabla u^T) + \left(\lambda_f - \frac{2}{3}\mu_f\right)\nabla \cdot u\mathbb{I} \qquad (17)$$

$\mathbb{I}$ represents the unit tensor, while λ_f and μ_f represent the fluid's volume and shear viscosity, respectively. Moving forward, the phase interaction force is given by:

$$F_{p-f} = -\frac{\sum_{p-1}^{N} F_{f-p}}{V_c} \qquad (18)$$

where V_c is the cell volume and N is the number of particles within it. F_{f-p} is the net force applied to the particles by the fluid. This force can be found by adding the forces acting on the particles that were previously presented.

$$F_{f-p} = F_d + F_{n,adh} + F_\tau + F_n^t + F_g + F_p \qquad (19)$$

The last two terms represent gravitational force and the force due to the pressure gradient, respectively.

4.4 CFD-DEM Coupling

During the simulation, the two solvers (CFD and DEM) work in parallel (Figure 6), so the number of processors used by each solver is the total number divided by two. When the simulation starts, the solution is initiated by the DEM time step calculation, then the initial flow regime is calculated by the CFD solver, and the data is then transferred to the DEM solver. After that, the DEM solver calculates the phase volume fraction and the interaction forces. Once this is done, the data is transferred to the CFD solver.

In the following part of the thesis, DEM will be replaced by Rocky (the software using DEM) and Fluent (the software using CFD).

Once the previous step is completed, Fluent will do a time step correction to obtain an integer multiple of Rocky's time step. Then the initial solid phase is updated in Fluent. The initial solid phase refers to the position and velocity of the solid particles. The next step is the parallel execution of one time step in Fluent and 'n' time steps in Rocky, where 'n' is the integer that was obtained in the previous step. This method is called sub-stepping, which allows multiple data exchanges during a Fluent time step. By increasing the Fluent time step size, the simulation time decreases without having a negative impact on the accuracy.

After the adjustment of each solver's time step and their execution, Rocky sends the first batch of data, which includes the transfer of the forces in semi-implicit form, then CFD calculates each parameter (velocity, pressure, physical properties) and sends the data to Rocky. Finally, these steps are repeated until the end of the simulation [32].

In the following figure, the flowchart of the coupling process is shown. The term "data exp" refers to data export, "data imp" to data import, and finally "data ex" to data exchange.

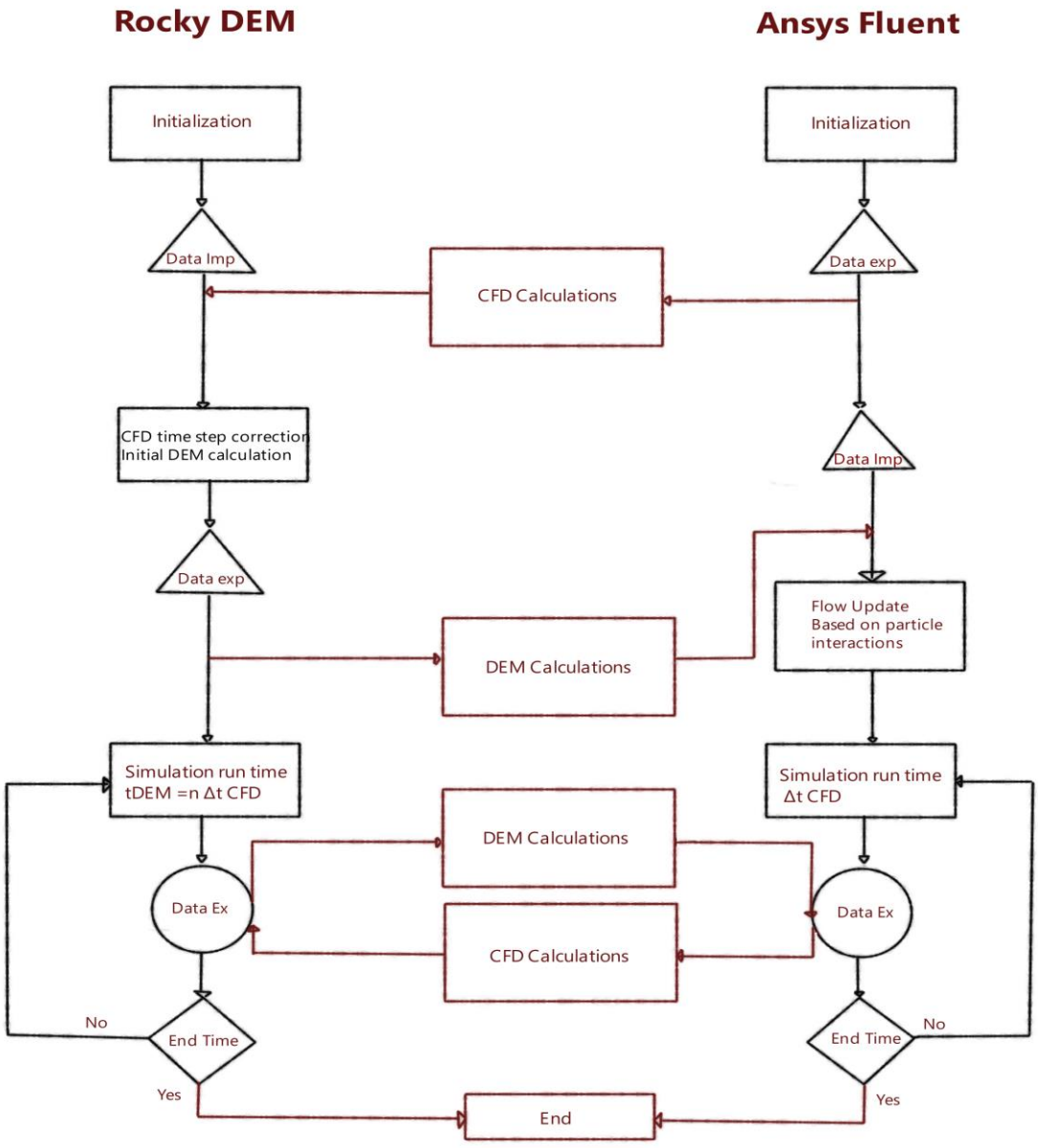

Figure 6: Flow chart of the CFD-DEM coupling scheme and working principle.

4.5 Particle Properties Definition

In this section, the parameters used in Rocky will be defined. As it has been mentioned previously, lactose particles were used in the simulations and experiments instead of the hemostatic powder.

In Table 2, the properties of the boundary (catheter wall) are shown. It's worth noting that the catheter wall was considered non-deformable.

Table 2: Material properties for the boundary.

Properties	Selected Value
Density (kg/m^3)	7850
Young's Modulus (GPa)	100
Poisson's ratio	0.3

With the properties of the boundary defined, we move on to the characterization of the lactose. The material properties of lactose are presented in Table 3.

Table 3: Material properties for lactose.

	Values	Range	Selected Value
Diameter (µm)	50 [40], 150-200 [41], 70 [12][13][14], 212-355 [42]	50 - 355	70
Density (kg/m^3)		1500-1525	1520
Young's Modulus (GPa)	0.005 [42],0.1 [40],0.2 [41], 1 [13][14], 9[12]	0.005-9	1
Poisson's ratio	0.3 [40], 0.35 [12] [13][14], 0.45 [41][42]	0.3-0.45	0.35
Coefficient of restitution	0.2 [41],0.1-0.8 [42],0.85 [12][13][14]	0.1-0.85	0.85
Sliding friction coefficient	0.3 [12], 0.4 [13], 0.45 [14], 0.5 [41],0.7 [40], 0.1-0.8 [42]	0.1-0.8	0.45
Rolling friction coefficient	0.05 [13][14], 0.1 [40], 0.3 [41], 0.1-0.8 [42]	0.05-0.8	0.05

It must be noted that the parameter sliding friction coefficient refers to static friction between two particles while the rolling friction coefficient refers to dynamic friction. Additionally, the resistance to deformation is represented by the stiffness ratio, while the coefficient of restitution estimates the particle energy dissipation after collision.

The selection of the values was performed based on the number of times they were previously used and the average values. More specifically, a parameter value would be chosen if it appeared in more than one paper (e.g. sliding friction coefficient), or in the case of a broad range of values, the average would be selected (e.g.Young's Modulus).

The particle mass flow rate was defined after estimating the mass of powder used during an experiment. More specifically, it was found that throughout most of the experiment, 10 g of powder was discharged from the sieve within 5 s, thus the powder flow rate was set at 2 g/s for all the simulations.

4.6 Conclusions

In this chapter, a detailed insight into the mathematical models for dense granular flow is given. The analysis commenced with the equations that describe particle-particle force and particle-boundary interaction and continued with fluid-particle interaction, covering the mathematical models that define the DEM model. The discussion proceeded with the governing equation of the CFD model, followed by a step-by-step explanation of the algorithm that defines the CFD-DEM coupling. Finally, a detailed analysis of the material properties used in this research was presented.

Chapter 5: Results and Discussion

5.1 Introduction

In this chapter, the results for both experiments and simulations will be presented. Our main goal is design optimization to obtain a successful powder delivery system. Additionally, the verification of numerical results for pressure drop over the catheter with the experimental results will be done.

5.2 Experimental Results

In this section, the experimental results will be presented. The analysis starts with effects of the design configuration on the powder flow behavior. The analysis continues with an examination of the effects of different air flow rates on pressure drop. To gain perspective on the problem, a reference case with a 0.37 m^3/h gas flow rate is presented.

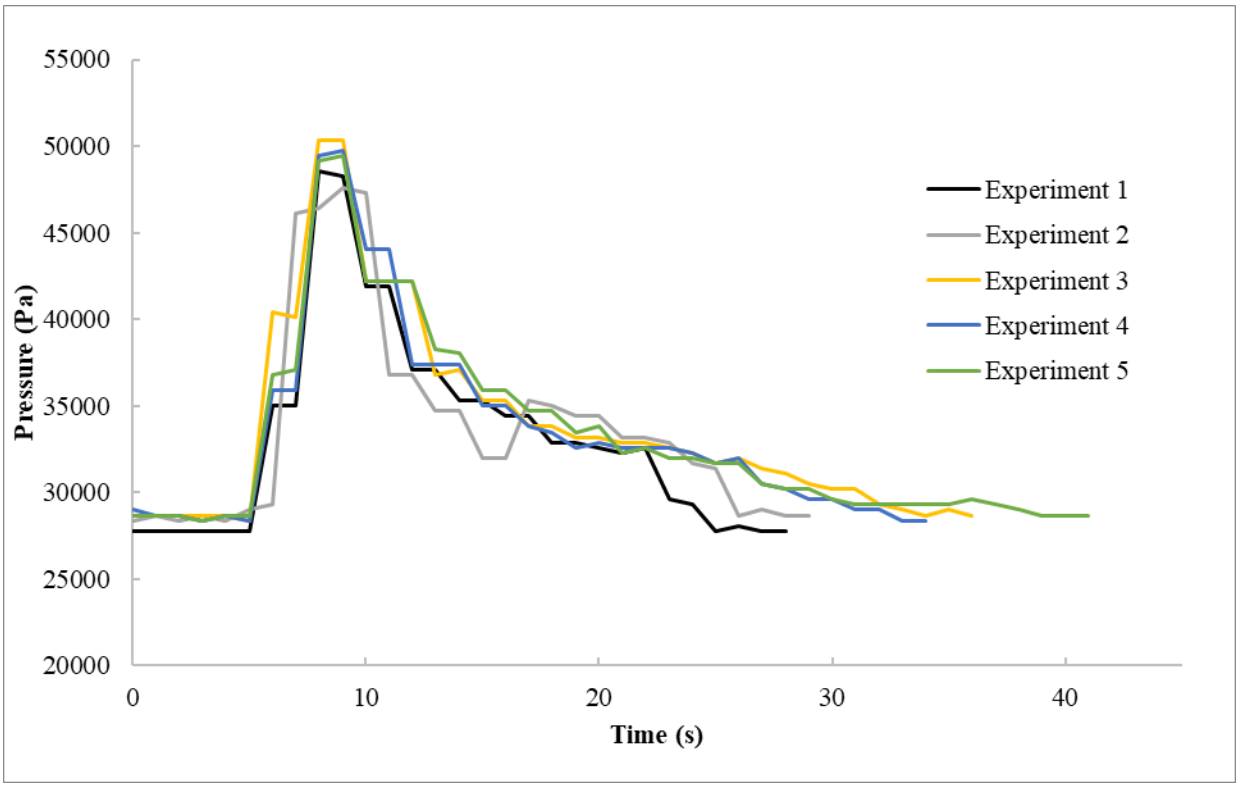

Figure 7: Pressure drop for the whole setup over time for a 0.37 m^3/h gas flow rate.

Figure 7 shows the pressure drop as a function of time for the whole experimental setup for the gas flow rate of 0.37 m^3/h. As mentioned in Chapter 3, the pressure was measured at a frequency of 1Hz. It can be seen that around the 10 s mark, the pressure drop increases greatly. This peak in the pressure drop indicates the start of the experiment. At this moment, the solenoid is activated, the sieve starts moving back-and-forth and forcing the particles out into the cyclone. The pressure drop spike lasts until the 15 s mark, roughly 5 s in total. By observing this behavior, we managed to estimate the powder mass flow rate. The sieve contains 10 g of powder, and it is emptied within 5 s, meaning that 2 g of powder are deposited in the cyclone every second. Once the sieve is empty, the pressure drop is reduced, but it does not reach the initial value. The reason behind this behavior is due to the motion of the particles within the catheter. Since the catheter is

1.47 m long, it takes more time for the particles to travel through it, causing the pressure drop fluctuations that can be seen after the 15 s mark.

5.2.1 Design Configuration Impact on Blockage and Mass Flow Rate

Flowability is used to describe how easily granular material can flow through silos [44]. In this project, the flow characterization for the different designs that were used will be defined by blockage. As mentioned in the introduction, our design needs to be robust. Thus, an ideal design must always be fully functional.

Table 4: Experimental data for different wall inclinations and radii.

Design	No of Trials	Length(mm)	Radius(mm)	Angle(α)	No of Blockages
1	5	50	27.5	61.50^o	2
2	5	60	27.5	65.38^o	1
3	5	70	27.5	68.55^o	0
4	5	100	27.5	74.62^o	5
5	5	76.88	33.5	66.46^o	0

To test each model's robustness, we ran 5 experiments for five different designs with a gas flow rate equal to 0.37 m^3/h. The first elimination of the designs was based on blockages. Any design which was characterized by at least one case of blockage was removed from the selection pool.

As shown in table 4, the only cases that showed no signs of blockage are designs 3 and 5 with a wall inclination of $\Theta = 21.45^{o}$ and $\Theta = 23.54^{o}$ (see Appendix A: Figure A1).

The reason behind the association of the wall inclination angle with the design efficiency derives from the work done on powder flowability through silos by Dietmar [44]. As stated in [44], the two parameters that determine a powder's flow conditions are the wall inclination and the wall friction angle. The wall friction angle is used as a measure of friction between bulk solids and the walls of silos. It can be observed that the wall friction is strictly dependent on the surface roughness. Since in this work every design was made with the same method (3D printed) and material, there will be no reference on the effects of wall friction angle on blockage.

Based on the results presented in Table 4, we can see the effects of length, radius, and angle on blockage. For example, in cases 1,2 and 4 where blockages appear, the behavior of the powder can be explained by the existence of stagnant zones created in the cyclone, as can be seen in Figure 8. For the first two cases, the short length of the cyclone does not allow the powder to flow continuously. This causes part of the powder to be deposited near the wall, creating a funnel flow within the cyclone, as seen in Figure 8. Case 4 is characterized by a small wall inclination angle, which creates a very steep conical geometry that leads to larger stagnation zones. This increase in the stagnation zone causes more particles to be deposited on the cyclone walls, which leads to higher friction forces. These forces slow down the flow within the cyclone and prevent the powder from flowing.

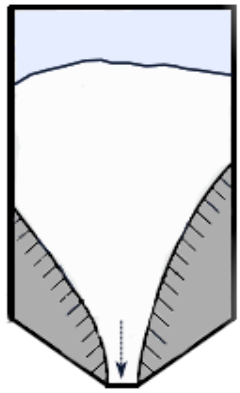

Figure 8: Funnel flow within a silo. The white region represents the particles in motion, while the gray region shows the stagnation zones where particles are trapped. The blue area is air.

The decision for the best design was made based on three parameters: the number of blockages that occurred, the total mass of powder that was delivered in the container of the setup, and the delivery time that powder needed to travel through the catheter and into the container. Both cases 3 and 5 showed no blockage and a total mass of powder deposition in the catheter equal to 9.5 ± 0.2 g. Case 5 was chosen as the best for our application, and details on its design can be found in Appendix A. The reason behind this decision is the powder mass flow rate, it was found that there was a 23% improvement in the delivering time of the powder through the catheter and into the container. In case 3, the powder was delivered within 21 s with a standard deviation of ± 0.1 s which was found from the measurements during the experiments, while in case 5, the powder was delivered within 16 ± 0.1 s The delivery time was measured during the 5 trials of each design using slow motion video capture to accurately observe the beginning and ending of the powder deposition in the container. As mentioned in Chapter 1, there is a time limit within which

the powder should be delivered; thus, for safety and efficiency, we chose the fastest case (case 5).

5.2.2 Pressure Drop vs. Gas Flow Rate

As mentioned before in this chapter, the effects of different flow rates on the total pressure drop will be presented. Experiments at different flow rates were conducted to test the robustness of the device. In order to allow the surgeon to adapt the flow conditions to each case separately, it was decided that the device should be tested for different flow rates.

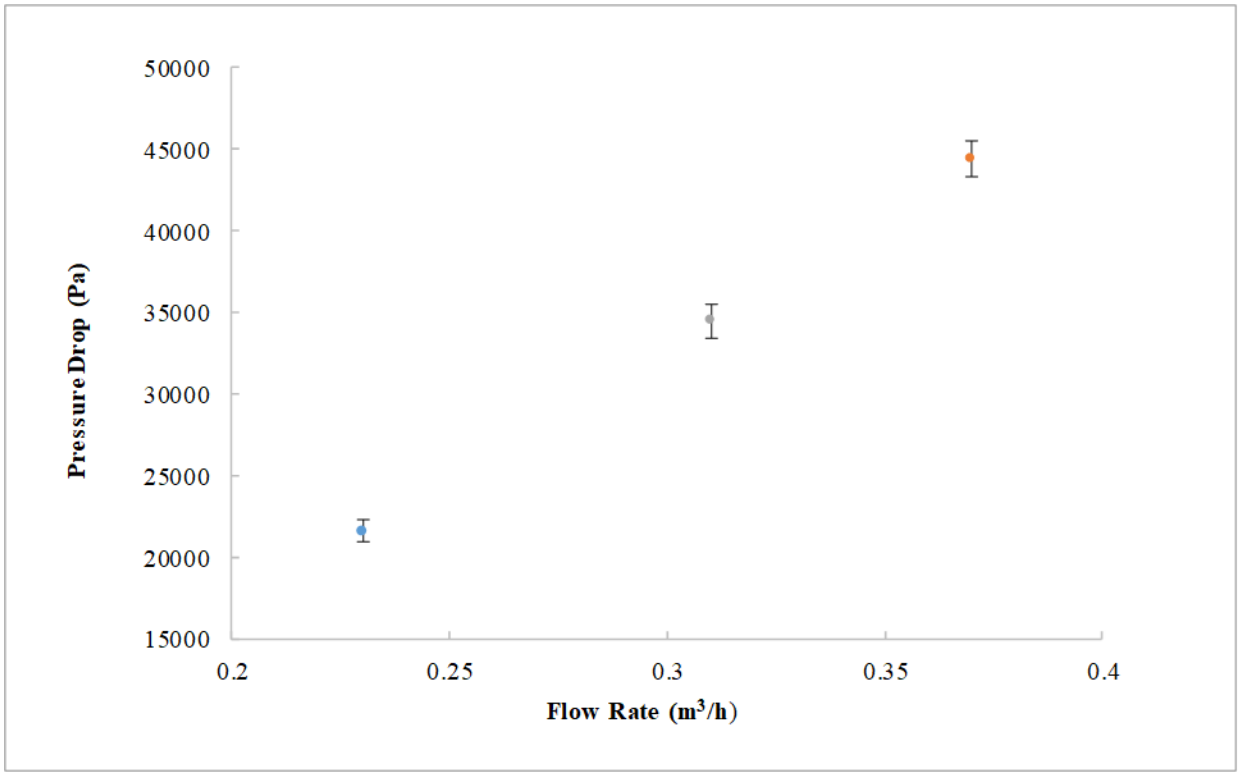

Figure 9: Air flow rate impacts pressure drop.

Figure 9 shows the pressure drop over the whole device, including the cyclone and the catheter. The pressure drop values across the catheter must be calculated. Five trials were performed for each gas flow rate. The experimental results can be found in Table 5, where the pressure drop values for each part of the experimental setup are presented.

Table 5: Pressure drop data for each part of the setup.

Flow rate(m^3/h)	Pressure drop in Setup (Pa)	Pressure drop in Cyclone (Pa)	Pressure drop in Catheter (Pa)	St. Deviation Catheter (Pa)
0.37	44394.17	8630.00	35764.17	3030.55
0.31	34505.36	5840.00	28665.36	1146.09
0.23	21604.90	3680.00	17924.90	951.04

The calculation of pressure drop through the catheter was achieved by calculating the losses for the cyclone and reducing them from the total losses that were found for the whole setup. To achieve that, five experiments were performed without the catheter. The container was attached directly to the cyclone. We used the same amount of powder that was selected for the experiments with the catheter to properly replicate the conditions. Once the solenoid started moving, we started recording the pressure drop values.

5.2.3 Particle Deposition and Mass Powder Efficiency

Even though this section does not have an immediate impact on the flow behavior, it does represent one of the most important parameters that defined the design. As mentioned in the introduction, to reduce the gas volume entering the stomach through the catheter, we must reduce the delivery time while delivering the necessary 5-7 g of hemostatic powder.

During the experiments, the sieve was filled with 10 g of non-compressed powder. An average of 9.5 ± 0.2 g was successfully transported while using chamber c as shown in Figure 4, chapter 3, while keeping the delivery time at 16 ± 0.1 sec as mentioned previously.

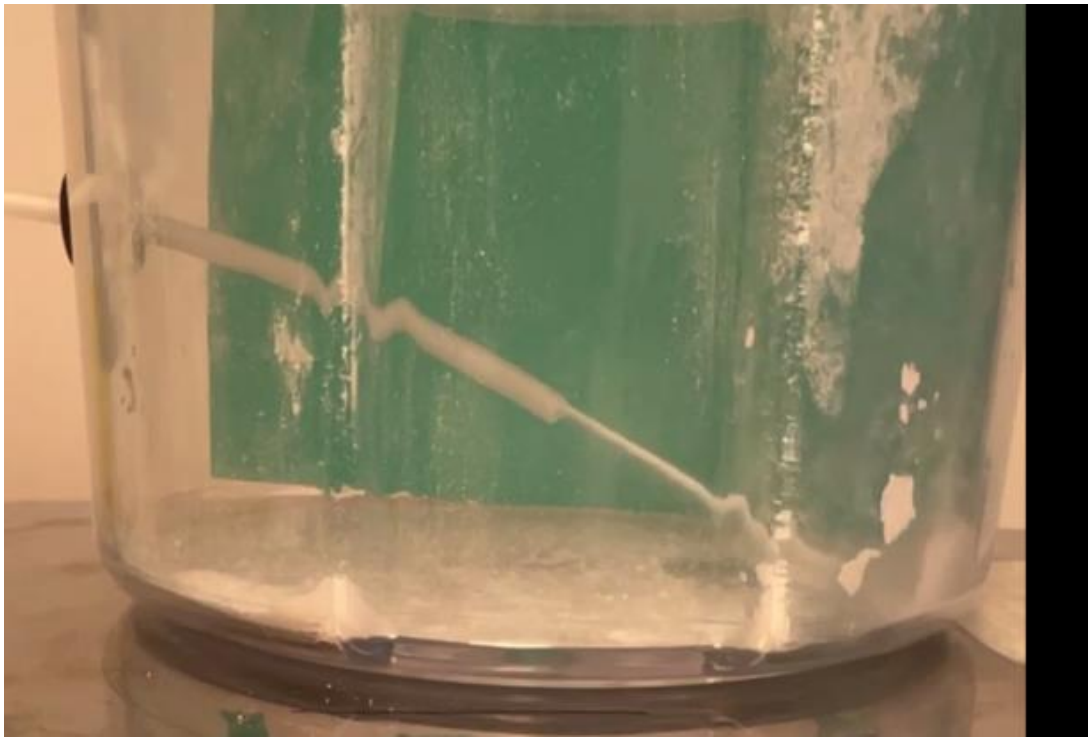

Figure 10: Particles flow at the outlet of the catheter at a 0.37 m^3/h air flow rate during experiments.

During the experiment for the case of 0.37 m^3/h air flow rate, the particle deposition of the powder was captured, as it can be seen in Figure 10. The powder was delivered through a continuous stream that can be directed to any point. This will allow surgeons to aim while operating and to prevent the powder from spreading randomly within the stomach.

5.3 Numerical set-up

There are numerous parameters that define simulations, with the most important being the mesh, which can be seen in Figure 11.

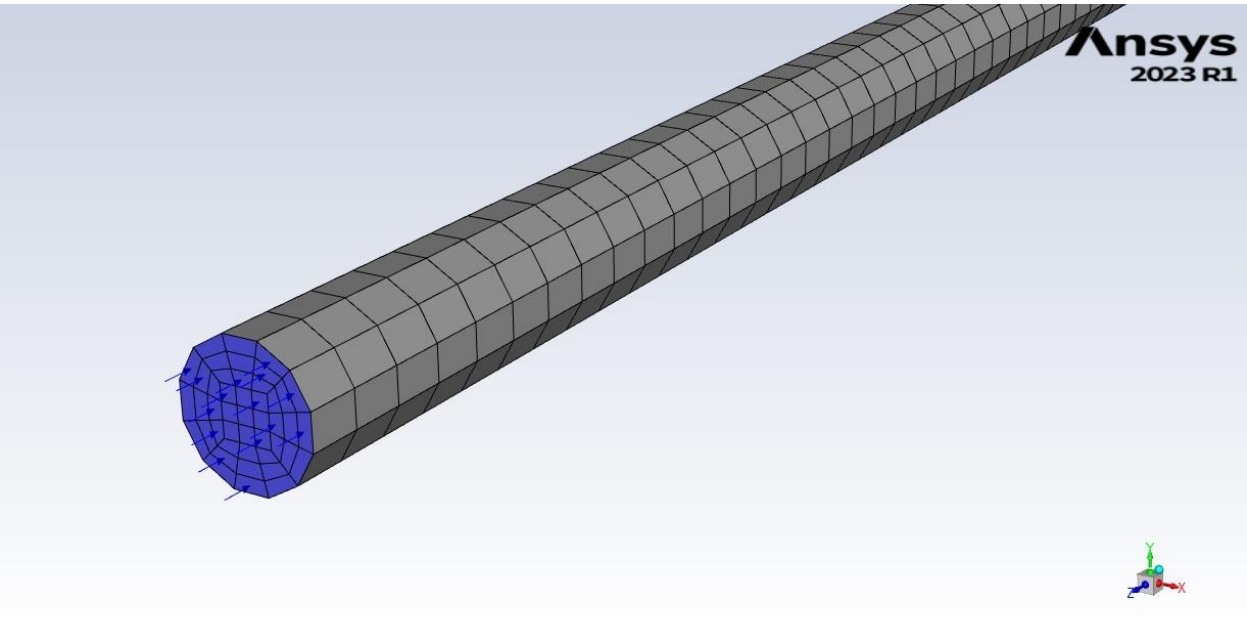

Figure 11: Mesh quality for the catheter is 0.002 m in diameter and 1.47 m in length.

The mesh was chosen to be coarse for the DEM to properly calculate the particle forces. As stated in [28], the element size should be two times larger than the smallest particle size. In this

work, the particles are 0.07 mm in diameter, while the catheter diameter is 2 mm. Thus, it was decided to keep the element size 2.38 times larger, adding a small safety factor, which led to 45 divisions on the face of the pipe. Additionally, on the length of the pipe, the total number of elements reached 135,000.

Since the geometry of a tube is simple, it was decided to use a structured mesh approach for the domain. To verify if the results of the simulations are mesh-independent, simple gas flow simulations were performed in Ansys Fluent.

The material used in both simulations and experiments was the same. We defined every parameter based on the material properties of lactose, which were shown in Chapter 4.

For the CFD part, Ansys Fluent was used, while for the DEM we used Rocky DEM. For the CFD setup, the following parameters were set:

- The SST k-ω model was chosen for the turbulent flow characterization, where default values were used.
- A velocity inlet was set based on the different experimental gas flow rates to examine the pressure drop through the catheter.
- The gas was air with properties that matched the experiments. For a room temperature of 20 ^{o}C: $\rho_f = 1.204$ kg/m^3 and $\mu_f = 18.13 \cdot 10^{-6}$ Ns/m^2.

The DEM setup can be narrowed down to the following steps:

- Implement material properties (Chapter 4)
- Set the powder mass flow rate to reflect the experiments (for example, 2 g/s)
- Set the mathematical models that describe the particle-particle and particle-boundary interactions (Chapter 4).
- Implement a coupling scheme.

- Determined CPU and GPU workloads. 12 processors were used for the CFD part, while the DEM calculations were performed on the GPU.

The convergence of the coupled simulations was determined by a time limit. The simulations were run up to 0.5 s with a time step of 0.002 s. It was determined that a steady state in the flow regime is reached within 0.5 s, as it can be seen in Figure 12.

With our system, a simulation like this would last 6-7 days for a powder mass flow rate of 2 g/s. The computational system consists of a 12th generation Intel Core i9-12900k 3.19 GHz processor, 64 GB RAM, and a Nvidia RTX 3070 Ti GPU.

5.4 Simulation Results

In this section, the results obtained from the simulations will be presented. To obtain comparable results between experiments and simulations, the powder mass flow rate was calculated using the pressure drop measurements. As will be seen in the following graphs, the time needed for a full powder discharge from the chamber is 5 s. Since the weight of the powder within the sieve was set to be 10 g, it can be assumed that, on average, the powder mass flow rate through the catheter is 2 g/s.

The simulations proceeded with respect to the experiments; thus, different flow rates and their effect on the pressure drop were examined. One parameter that differentiates the simulations from the experiments is particle morphology. As mentioned earlier, the particles in the simulation are considered to be spherical, while the particles in the experiment were not. The significance of particle morphology in the flow regime will not be examined.

The result presentation will start with one of the cases, which will be considered a baseline for the rest of the experiments.

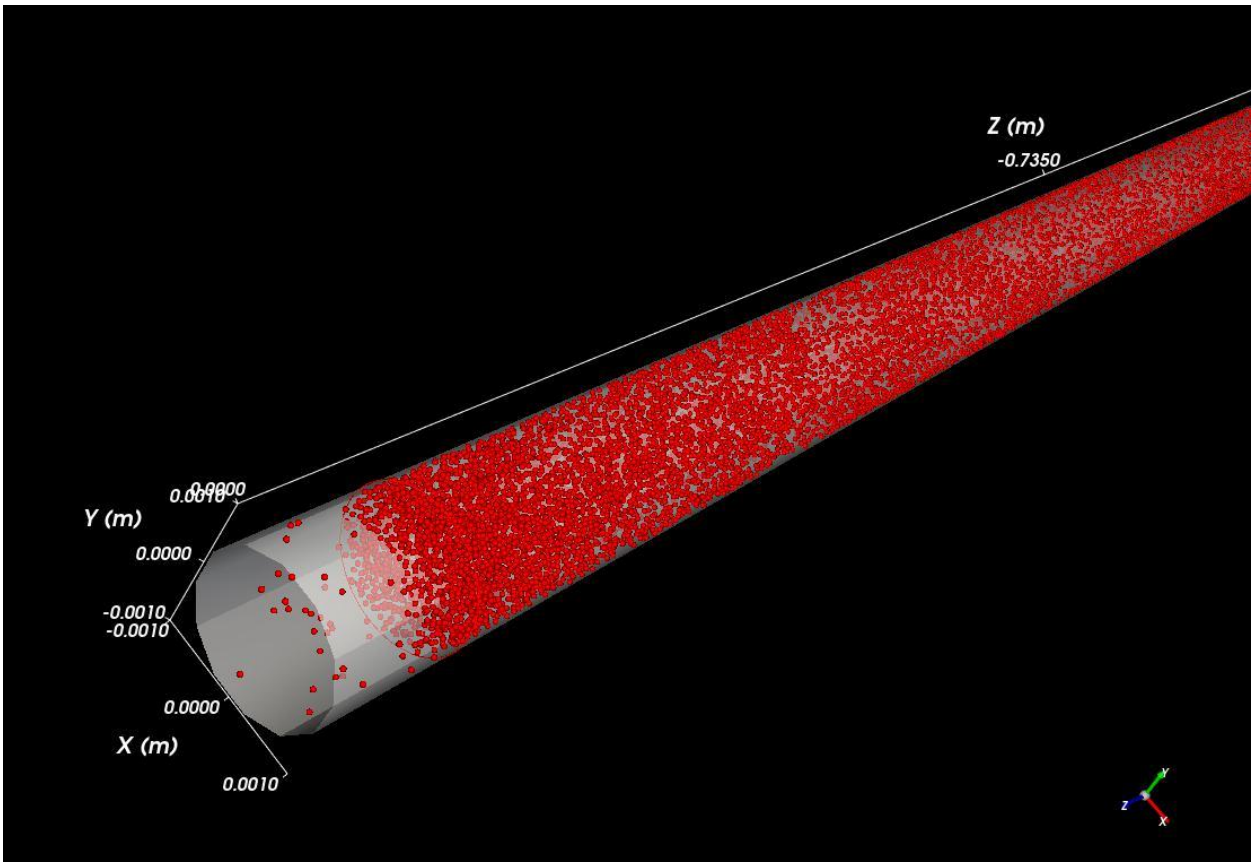

Figure 12: Particle flow within the catheter during the CFD-DEM numerical solution.

Figure 12 shows the particles moving within the catheter. In this specific case, the flow rate is set to 0.37 m^3/h. The total number of particles for this setup is 1.7 million.

5.4.1 Pressure Drop Over Time

As has been established from the previous analysis, the validation of experiments with respect to the simulations will be done only through the pressure drop measurements.

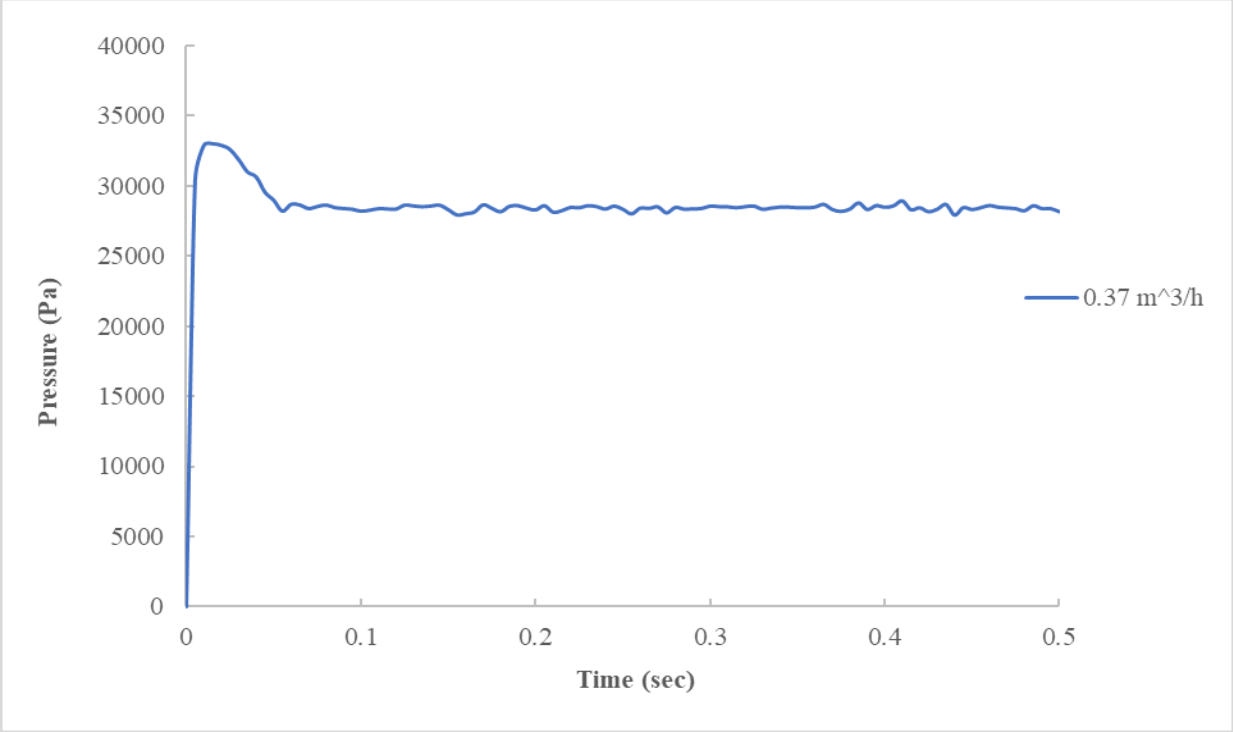

Figure 13: Pressure drop over time for an air flow rate of 0.37 m^3/h.

Figure 13 shows the pressure drop over time. As it can be seen, the average pressure is 28.39 kPa. For the case of an air flow rate of 0.37 m^3/h, the Reynolds number, Re = 4344 (calculated based on the air velocity at the inlet of the device), shows that the flow is turbulent. The oscillations in the pressure are characteristic of gas-solid flows [34]. Depending on the flow (suspension, stratified, dune), these oscillations change in amplitude and frequency. Previous work in the field shows that it is possible to predict flow behavior based on the produced signal

[35]. The simulations were done for different air flow rates of 0.42 m^3/h, 0.31 m^3/h, and 0.23 m^3/h, to investigate the effects of different flow rates on pressure drop.

5.4.2 Pressure Drop vs. Air Flow Rate

To examine the impact of flow rates on the pressure drop, four cases were considered, as can be seen in Figure 14.

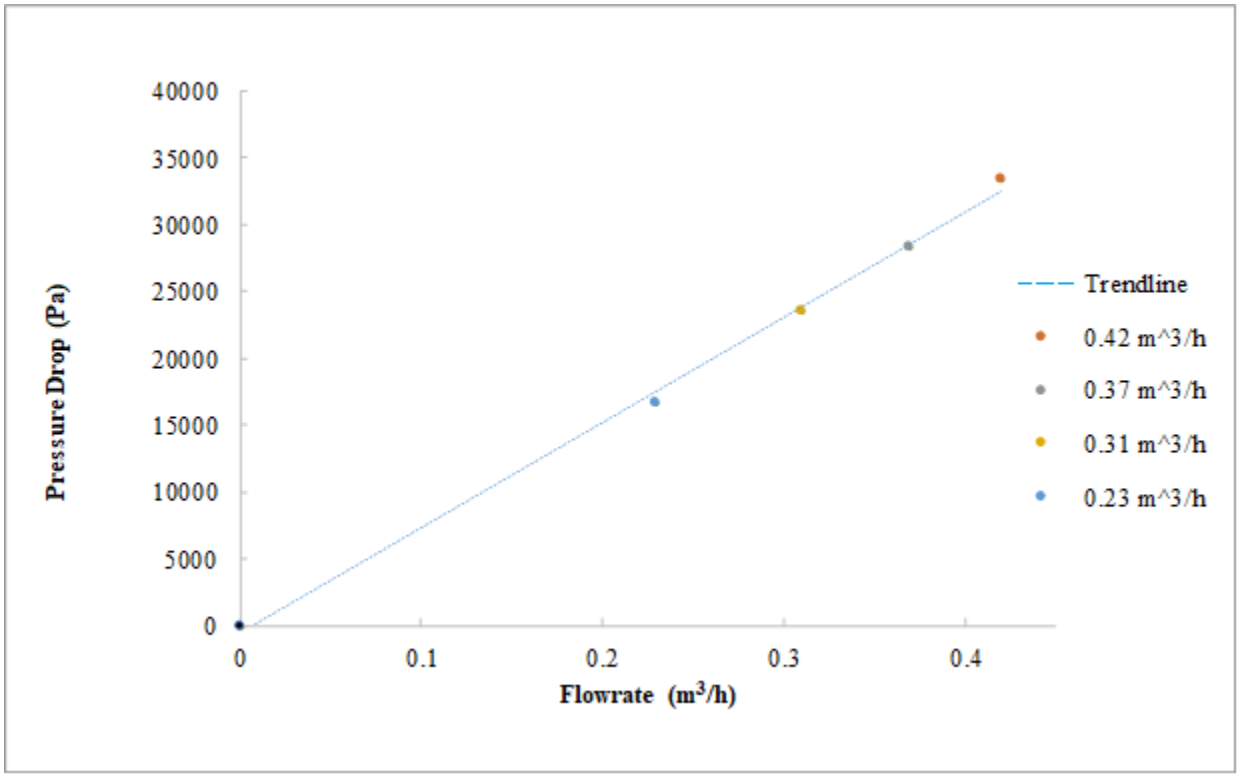

Figure 14: Pressure drop for different gas flow rates.

The data points can be fitted by the following linear equation:

$$y = A \cdot x - B \ , \quad R^2 = 0.9968 \qquad (20)$$

Where $y = \Delta p$ is the pressure drop, x = $\dot{V}_g$ is the powder volumetric flow rate.

A = $283.37 \cdot 10^6 \cdot \frac{Ns}{m^5}$, B = $528.6 \cdot \frac{N}{m^2}$. In Table 6 the results of the average pressure drop for different flow rates are presented.

Table 6: Average pressure drop for different gas flow rates.

Gas Flow rate (m^3/h)	Average Pressure Drop (Pa)
0.21	16616.48
0.31	23601.80
0.37	28393.43
0.42	33433.04

5.4.3 Solid Volume Fraction

The importance of solid volume fraction is related to the interaction between particles and flow. As stated in [20], when the solid or particle volume fraction $\alpha_i \geq 10^{-3,}$ the flow can be considered dense; if $\alpha_i \leq 10^{-6,}$ the particles have no effect on the flow. The volume fraction, as calculated by

Rocky DEM, can be seen in the figure below. The solid mass fraction is around 0.068, which is greater than $10^{-3,}$ confirming the powder's dense nature.

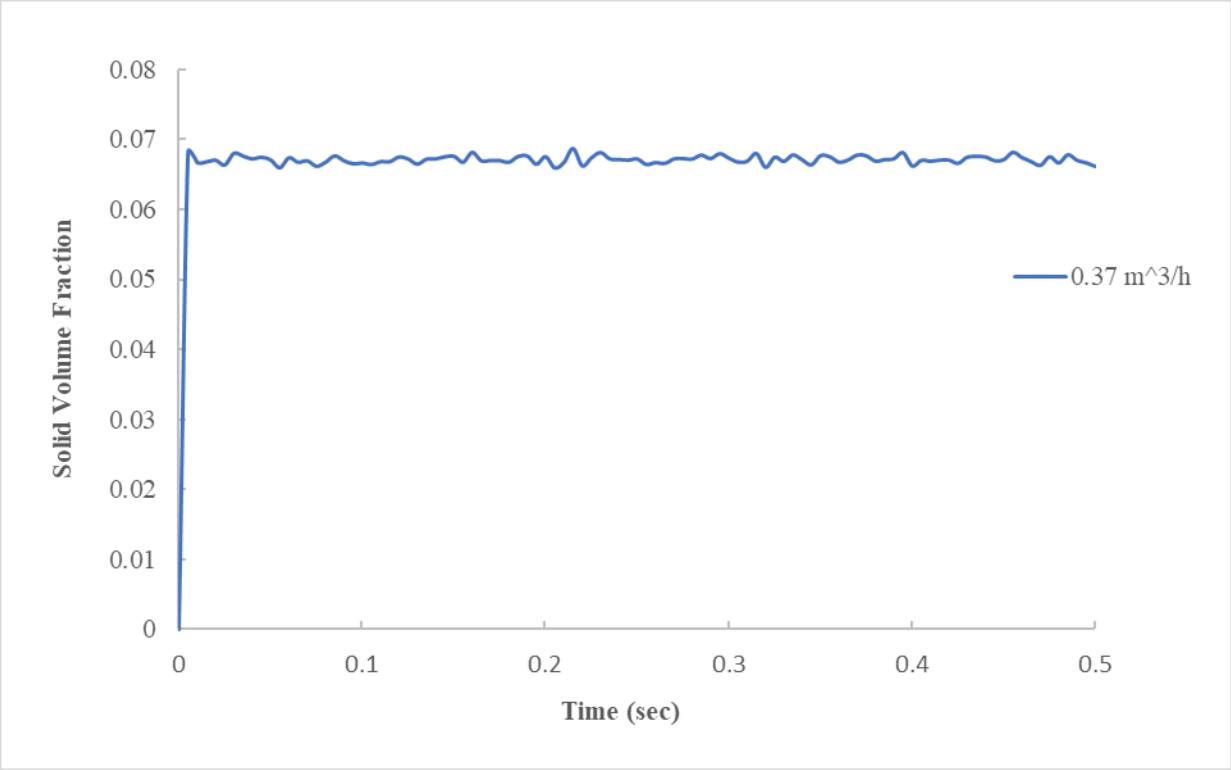

Figure 15: The inlet solid volume fraction behavior over time for the case of a 0.37 m^3/h air flow rate.

The oscillations shown in Figure 15 derive from the unconstrained height of the lactose particles within the tube. As a mass of powder enters the catheter, unconstrained particles are swayed by the high velocity flow, forcing them to move in different directions, while other particles might be deposited on the tube walls. Since the mass and momentum conservation equations are connected to the fluid volume fraction, which is also fluctuating, the pressure-drop graph also shows these oscillations.

5.4.4 Pressure Drop vs. Powder Flow Rate

The final set of simulations examined the effects of different powder mass flow rates on the pressure drop. To have a clear image, the gas flow rate was kept constant in each experiment (0.37 m^3/h).

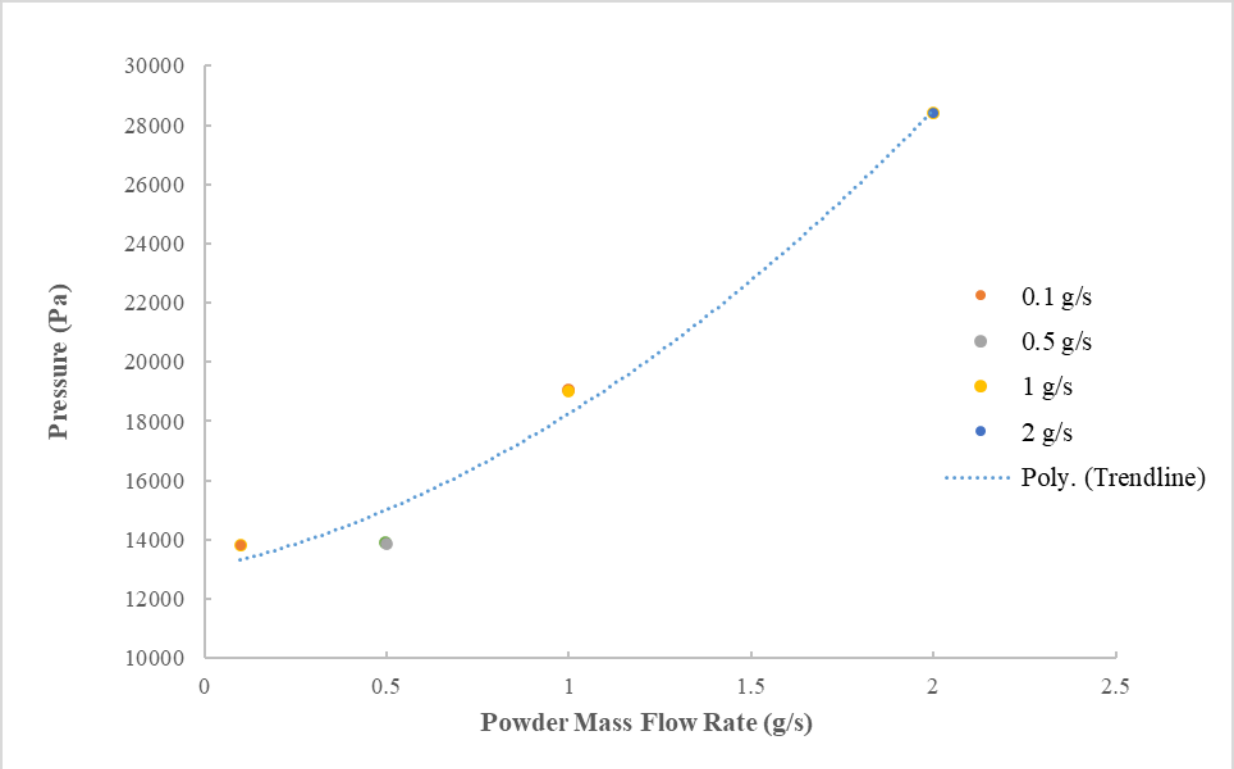

Figure 16: Pressure drop as a function of powder mass flow rate for 0.37 m^3/h gas flow rate.

Three cases were run with a powder mass flow rate of 0.1 g/s, 0.5 g/s, 1 g/s, and finally, 2 g/s, and the pressure drop results can be found in Figure 16. A second-order polynomial expression was found to fit the pressure drop as a function of particle mass flow rate:

$$y = Ax^2 + B \cdot x + C \ ,$$

$$R^2 = 0.9847 \qquad (21)$$

where y = Δp, x = $\dot{m}_p$ which is powder mass flow rate, A = $2505.2 \cdot 10^6 \cdot \frac{1}{m\ kg}$,

B = $2737.3 \cdot 10^3 \cdot \frac{1}{m\ s}$ and C = $13019 \cdot \frac{kg}{m\ s^2}$.

5.5 Simulations vs. Experiments

Since the results of each section have been analyzed (Table 7), it is crucial to compare them (Figure 17) and examine how accurately the CFD-DEM analysis can replicate the experimental results. More specifically, it is needed to examine if the mathematical modeling that was described in Chapter 4 can be used for small geometry and high-velocity granular flows.

It can be seen that the results of both experiments and simulations are very close when the inlet flow rate is lower, while the difference between them increases as the flow rate increases. Finally, a linear correlation can be observed between the data points of both simulations and experiments.

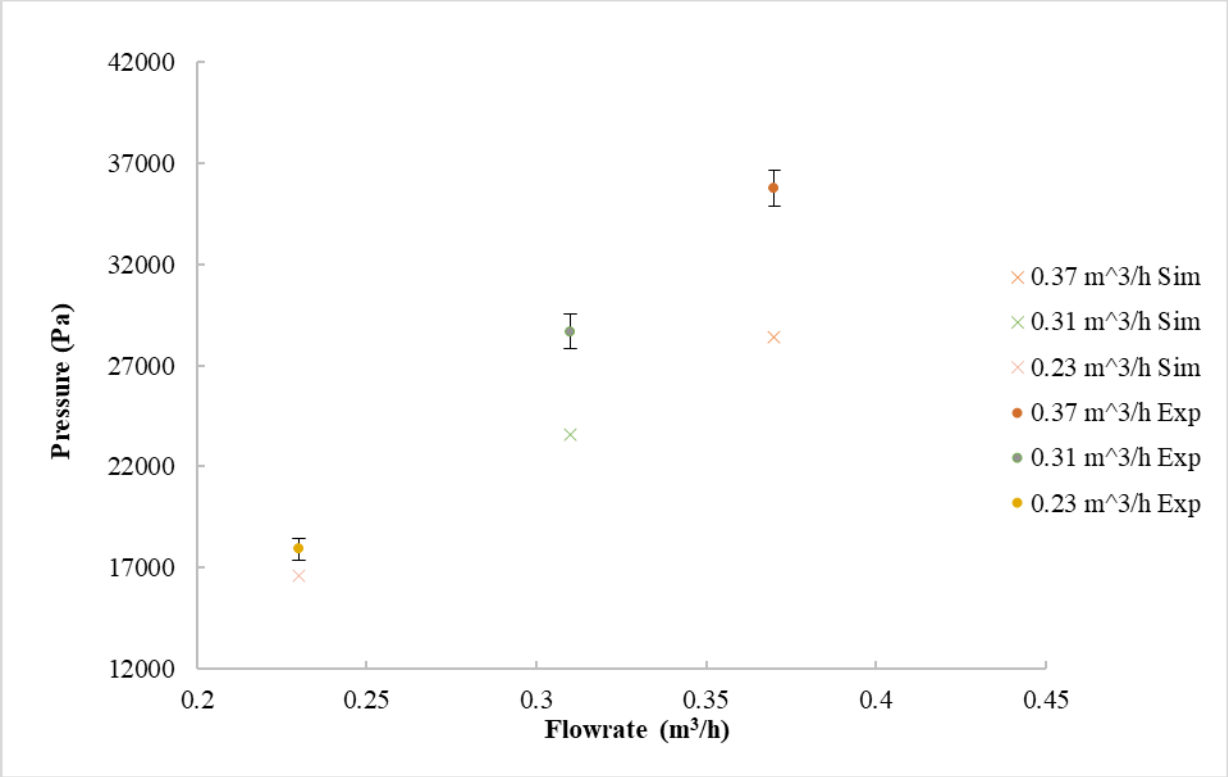

Figure 17: Experimental results vs. simulation results.

Table 7: The deviation between experiments and simulations.

Gas Flow rate (m^3/h)	Pressure drop in exp (Pa)	Pressure drop in sim (Pa)	Value Deviation %
0.37	35764.17	28393.43	20.60
0.31	28665.36	23601.80	17.66
0.23	17924.90	16616.48	7.30

5.6 Qualitative Error Analysis

Both experimental and numerical approaches generate errors, some of which are unavoidable. The first set of errors refers to simplifications between simulations and experiments. For example, the catheter is bent in the experiments (see Figure 2), but in the simulations, the bending was neglected. Furthermore, the catheter's surface roughness changed every time since there were particles deposited on the catheter's walls. Additionally, the inlet in the simulation was set as a uniform source of solid particles with a steady flow, which was not the case for the experiments, where the flow at the inlet of the catheter was not uniform and the flow rate was time-dependent.

Another factor that contributes to the differences between experimental and numerical results is that only the catheter was considered in the simulations. Therefore, the air flow and complex particle collisions during the mixing of the powder through the cyclone were not considered. Despite the fact that the pressure drop values were adjusted for the catheter only in the experimental results, the simulation of the device would lead to more accurate results. Additionally, there is a limitation introduced by the coupling system between Ansys Fluent and Rocky DEM where the element size of the mesh must be at least two times larger than the particle size. Since the diameter of the catheter is 2 mm and the particle size was considered to be 70 um the mesh that was chosen was a coarse one. The other parameter that might influence the flow regime is particle morphology. During the simulation, the particles were considered spherical, but during the experiments, they were not.

Furthermore, reading errors are introduced in the results. The gas flow regulator consists of the traditional ball-bearing reading. The metal bearing is adjusted to the flow rate required for the

experiments using visual means. Since the human eye as well as the readings on the regulator itself are not very precise, a difference between the actual flow rate and the one considered is expected. Finally, as mentioned in Chapter 3, the sensor is defined by a ± 0.075% accuracy. The model that was chosen has a reading range between 0-36 psi, meaning that the error produced by the sensor is ±186 Pa. It has now become apparent that the errors derived from sensor accuracy do not have a big role in the value deviation between experiments and simulations.

5.7 Conclusions

In this chapter, the numerical and experimental results are presented. In the experiments, the effects of different designs on powder flowability were discussed, while an investigation on the effects of flow rate on the pressure drop was examined. It was shown that the pressure drop changes linearly with the air flow rate and non-linearly with the powder mass flow rate. The current flow conditions and performance of this prototype showed its advantages over the previous devices that were mentioned in Chapter 1. Similar results, for a lower inlet gas flow rate, for the experimental and numerical simulation results, along with the linear relation between pressure drop and gas mass flow rate, indicate the potential strength of the CFD-DEM 4-way coupling approach.

Chapter 6: Conclusion

6.1 Summary

This study focused on the development of turbulent dense granular flows using a system coupling the CFD and DEM methods to find the optimal conditions for the delivery of hemostatic powders in the interior of a human stomach. A prototype for laboratory testing was built to efficiently deliver adhesive medicinal powders through a catheter. The prototype was manufactured using 3D printing and was designed to accommodate turbulent, dense granular flows.

Once the design was completed, a detailed insight into the mathematical models for dense granular flows was presented. The purpose of this chapter was the introduction of particle and fluid models that could reproduce the experimental approach. The analysis commenced with the equations that describe particle force interaction with other particles and boundaries, along with fluid particle interaction, covering the mathematical models that define the DEM model. The discussion proceeded with the governing equation of the CFD model, followed by a step-by-step explanation of the algorithm that defines the CFD-DEM coupling and concluding with a detailed analysis of the material properties that defined this research.

In the final part, an investigation of the behavior of high-velocity dense granular flows in numerical simulations (Ansys Fluent and Rocky DEM) and experiments was conducted. In the experimental part, the impact of the cyclone design on the flowability was presented, along with the flow conditions of the powder at the outlet of the catheter. It was reported that the flow conditions achieved using a continuous flow approach created the ideal conditions for future in

vivo experiments. In the numerical part, the behavior of the pressure and solid volume fraction with respect to time over the catheter was examined. For both experiments and simulations, an investigation on the effects of gas flow rates and powder mass flow rate on the pressure drop over the catheter was conducted while examining the efficiency of the powder delivery system based on blockage and the total powder mass delivered. It was concluded that the numerical simulations using CFD-DEM coupling were able to predict very well the experimental results for a lower inlet gas flow rate (7%) with an increase in the difference (20%) for a higher gas flow rate.

6.2 Contribution

The current study aims to offer an alternative solution to the treatment of UGIB by creating a medical device prototype capable of working in a laboratory environment. The device was initially designed to facilitate the main tasks that were mentioned in Chapter 1. The prototype is capable of safely delivering adhesive powders through a 2 mm catheter in an enclosed domain replicating a human stomach while producing a continuous flow that significantly reduces any potential blockage. The powder delivery system was built to facilitate various surgical cases. Thus, the design was tested under different conditions to respect the surgical requirements that the Kastrup team provided.

To achieve these goals, it was essential to analyze high-velocity granular flows. The verification of the experimental results was performed with the recently developed method of 4-way coupling between CFD and DEM.

6.3 Limitations

In this work, there are some limitations. Some of them have already been mentioned in Chapter 5. Here we will add more limitations with respect to the numerical simulations. The most important one is the lack of mesh options. The mesh choices were very limited due to the restrictions of the DEM solver. It is stated [28] that the mesh cell size should be at least 2 times larger than the particle size for the solver to accurately calculate the particle-particle forces. Due to the limited space (diameter of 2 mm), the mech introduces errors in the simulation results. Another limitation that refers to simulations is derived from the lack of computational power of our systems. Since the study of these types of flows introduces millions of particles flowing in a 1.47-meter-long catheter in a CFD-DEM simulation, it was computationally very challenging to implement a simulation for the whole setup. As mentioned in chapter 5, the current case study would take 6-7 days per simulation with only the catheter. By eliminating the rest of the setup, the study proceeded in a relatively quick way but introduced errors.

6.4 Future Work

Looking into the future, there are a few steps forward that need to be taken to take this project to the next level. As pointed out in Chapter 3, it would be beneficial for the cyclone optimization to numerically solve the whole setup. Since the cyclone design was chosen experimentally, it would be safe to assume that the current design is not optimal. As mentioned in Chapter 5, the optimal inclination angle can be found between [21^o, 24^o]. By implementing this part in the simulations, it would be easier to see and control the powder mixing in a way that the losses and the possible

particle collisions and deposition on the walls will be reduced**, l**eading to a highly optimized powder flow with high powder delivery efficiency.

Furthermore, the device in which the experiments were conducted is just a prototype, meaning that at its current state, the device does not meet surgical standards. There is a need for a few modifications, as pointed out by the doctors that are collaborating with our group, to proceed to the testing phase. A few of these changes are:

- Test the prototype with the hemostatic powder.
- Change the cyclone material from resin to something robust.
- Animal testing. Verify that the device can work in surgical environment.

Bibliography

[1] Chad T. Whelan, MD1.Connie Chen, PharmD2, Peter Kaboli, MD, MS3,4Juned Siddique, DrPH5,Micah Prochaska, BA, David O. Meltzer, MD, PhD. *Upper Versus Lower gastrointestinal Bleeding: A Direct Comparison of Clinical Presentation, Outcomes, and Resource Utilization*. Society of Hospital Medicine, 2010 DOI 10.1002/jhm.606

[2] M.E. van Leerdam MD, PhD. *Epidemiology of acute upper gastrointestinal bleeding*. Best Practice & Research Clinical Gastroenterology Vol. 22, No. 2, pp. 209–224, 2008, doi:10.1016/j.bpg.2007.10.011

[3] Amrit K. Kamboj, MD; Patrick Hoversten, MD; and Cadman L. Leggett, MD. *Upper Gastrointestinal Bleeding: Etiologies and Management*, Mayo Clin Proc. April 2019, https://doi.org/10.1016/j.mayocp.2019.01.022

[4] Louis H. S. Lau, Joseph J. Y. Sung. *Treatment of upper gastrointestinal bleeding in 2020: New techniques and outcomes*. Digestive Endoscopy 2021. doi: 10.1111/den.13674

[5] J. J. Y. Sung, D. Luo, J. C. Y. Wu, J. Y. L. Ching, F. K. L. Chan, J. Y. W. Lau, S. Mack, R. Ducharme, P. Okolo,M. Canto, A. Kalloo4 S. A. Giday . *Early clinical experience of the safety and effectiveness of Hemospray in achieving hemostasis in patients with acute peptic ulcer bleeding.* Endoscopy, 2011

[6] G.F.B.A. Kaehler, M.G. Sold, K. Fischer, S. Post, M. Enderle. *Selective Fluid Cushion in the Submucosal Layer by Water Jet: Advantage for Endoscopic Mucosal Resection*. Eur Surg Res 2007. DOI: 10.1159/000099597

[7] Teruo HOSHINO, Toru ENDO, Koji KUSAKARI and Masashi ISHIDA. *Gastric Mucosal Injury by Transendoscopic Compressed Air Delivery of Powdered NaCl, KCl or NSAIDs in Dogs*. Dig. Endosc., 1993

[8] G F Longstreth, *Epidemiology of hospitalization for acute upper gastrointestinal hemorrhage: a population-based study,* Am J Gastroenterol. 1995 Feb;90(2):206-10. PMID: 7847286.

[9] Brandon AWuerth, Don C. Rockey *Changing Epidemiology of Upper Gastrointestinal Hemorrhage in the Last Decade: A Nationwide Analysis*, Dig Dis Sci. 2018 May;63(5):1286-1293. doi: 10.1007/s10620-017-4882-6. Epub 2017 Dec 27. PMID: 29282637

[10] Alexander M. DiGregorio, Heidi Alvey *Gastrointestinal Bleeding*, 2023 Jun 5. In: StatPearls [Internet]. Treasure Island (FL): StatPearls Publishing; 2023 Jan–. PMID: 30725976.

[11] Jill Henley1 and Jerry D. Brewer2 *Review Article Newer Hemostatic Agents Used in the Practice of Dermatologic Surgery* Hindawi Publishing Corporation Dermatology Research and Practice Volume 2013, http://dx.doi.org/10.1155/2013/279289

[12] Berend van Wachem, Kyrre Thalberg, Johan Remmelgas, and Ingela Niklasson-Bjeorn *Simulation of Dry Powder Inhalers: Combining Micro-Scale, Meso-Scale and Macro-Scale Modeling*, AlChe J., 2016 DOI 10.1002/aic.15424

[13] Duy Nguyen, Johan Remmelgas, Ingela Niklasson Björn, Berend van Wachem, Kyrre Thalberg *Towards quantitative prediction of the performance of dry powder inhalers by multi-scale simulations and experiments*, Int J Pharm. 2018 Aug 25;547(1-2):31-43. doi: 10.1016/j.ijpharm.2018.05.047, Epub 2018 May 21. PMID: 29792988.

[14] Mostafa Sulaiman , Xiaoyu Liu, Sankaran Sundaresan *A CFD-DEM investigation of powder transport and aerosolization in ELLIPTA® dry powder inhaler* Powder Technology 409, 2022 https://doi.org/10.1016/j.powtec.2022.117817

[15] Nabil Ali-Mohamad, Massimo Cau , James Baylis, Veronika Zenova , Hugh Semple , Andrew Beckett , Andrew McFadden , Fergal Donnellan , Christian Kastrup, *Severe upper gastrointestinal bleeding is halted by endoscopically delivered self-propelling thrombin powder: A porcine pilot study*, Endosc Int Open. 2021 May;9(5):E693-E698. doi: 10.1055/a-1374-5839. Epub 2021 Apr 22. PMID: 33937509; PMCID: PMC8062227.

[16] Christopher E. Brennen, *Fundamentals of Multiphase Flow*, Cambridge University Press 2005, DOI: https://doi.org/10.1017/CBO9780511807169

[17] K. Kesava Rao, Prabhu R. Nott, *An Introduction to Granular Flow*, Cambridge University Press 2008, DOI: https://doi.org/10.1017/CBO9780511611513

[18] E. Teunou, JJ Fitzpatrick, *Effect of storage time and consolidation on food powder flowability*, Journal of Food Engineering vol 43, 2000, DOI: https://doi.org/10.1016/S0260-8774(99)00137-5

[19] Jenike, A. W. (1964). *Storage and flow of solids*, University of Utah, revised in 1980

[20] Mahmoud A. EI-Emam, Ling Zhou, Eldong Shi, Chen Han, Ling Bai, Ramesh Agawal, *Theories and Applications of CFD-DEM Coupling Approach for Granular Flow: A Review*, Arch Computat Methods Eng 28, 2021, https://doi.org/10.1007/s11831-021-09568-9

[21] J. Ding, D. Gidaspow, *A bubbling fluidization model using kinetic theory of granular flow*, AIChE J. 3, 1990

[22] X.-Z. Chen, D.-P. Shi, X. Gao, Z.-H. Luo, *A fundamental CFD study of the gas–solid flow field in fluidized bed polymerization reactors*, Powder Technol. 205, 2011

[23] N. Zhang, B. Lu, W. Wang, J. Li, *3D CFD simulation of hydrodynamics of a 150MWe circulating fluidized bed boiler*, Chem. Eng. J. 162, 2010

[24] A. Nikolopoulos, N. Nikolopoulos, A. Charitos, P. Grammelis, E. Kakaras, A.R. Bidwe, G. Varela, *High-resolution 3-D full-loop simulation of a CFB carbonator cold model*, Chem. Eng. Sci. 90, 2013

[25] Ansys® Academic Research Fluent, Release 23.1, Help System, Ansys Fluent Theory Guide, ANSYS, Inc

[26] Xizhong Chen, Junwu Wang, *A comparison of two-fluid model, dense discrete particle model and CFD-DEM method for modeling impinging gas–solid flows*, Powder Technology 254, 2014

[27] Y. Tsuji, T. Kawaguchi and T. Tanaka, *Discrete particle simulation of two-dimensional fluidized bed*, Powder Technology 77, 1993

[28] Ansys® Academic Research Rocky, Release 23.1, Help System, DEM TECHNICAL MANUAL, ANSYS, Inc

[29] M. Xu, F. Chen, X. Liu,W. Ge, J. Li, Discrete particle simulation of gas–solid two-phase flows with multi-scale CPU-GPU hybrid computation, Chem. Eng. J. 207, 2012 746–757

[30] Muhammad Adnan, Jie Sun, Nouman Ahmad, Jin Jia Wei *Comparative CFD modeling of a bubbling bed using a Eulerian–Eulerian two-fluid model (TFM) and a Eulerian-Lagrangian dense discrete phase model (DDPM)*, Powder Technology 383, 2021

[31] Alvaro Janda, Jin Y. Ooi, *DEM modeling of cone penetration and unconfined compression in cohesive solids*, Powder Technology 293, 2016

[32] Ansys® Academic Research Rocky, Release 23.1, Help System, CFD_COUPLING_ TECHNICAL MANUAL, ANSYS, Inc

[33] W.K. Hiromi Ariyaratne, E.V.P.J. Manjula, Chandana Ratnayake, Morten C. Melaaen, *CFD Approaches for Modeling Gas-Solids Multiphase Flows– A Review*, Proceedings of The 9th EUROSIM Congress on Modelling and Simulation, EUROSIM 2016, The 57th SIMS Conference on Simulation and Modelling SIMS, 2016, DOI: 10.3384/ecp17142680

[34] Zhen Miao, Shibo Kuang, Habib Zughbi, Aibing Yua, *Numerical simulation of dense-phase pneumatic transport of powder in horizontal pipes*, Powder Technology 361, 2020

[35] Shrikant V. Dhodapkar and George E. Klinzing, *Pressure fluctuations in pneumatic conveying systems*, Powder Technology 74, 1993

[36] Massimo F. Cau, Nabil Ali-Mohamad, James R. Baylis, Veronika Zenova , Adele Khavari , Nuoya Peng, Andrew McFadden, Fergal Donnellanc , Daniel R. Owen, David F. Schaeffer, Chandrasekaran Nagaswamie , RustemI. Litvinov JohnW. Weisel Joao Rezende-Neto Hugh A. Semple, Andrew Beckett, ChristianJ. Kastrup, *Percutaneous delivery of self-propelling hemostatic powder for managing non-compressible abdominal hemorrhage: a proof-of-concept study in swine*, Injury 53,2022

[37] Bahman Zohuri, *Thermal-Hydraulic Analysis of Nuclear Reactors*, Springer, 2017

[38] Baojiang Sun, *Multiphase Flow Model for Well Drilling*, Wiley,2016, DOI:10.1002/9781118720288

[39] Liang-Shih Fan, Chao Zhu, *Principles of Gas-Solid Flows*, Cambridge University Press, 1998, DOI: https://doi.org/10.1017/CBO9780511530142

[40] Ryosuke Mitani, Shuji Ohsaki, Hideya Nakamura, Satoru Watano, Numerical *Study on Particle Adhesion in Dry Powder Inhaler Device,* Chem Pharm Bull (Tokyo). 2020;68(8):726-736. doi: 10.1248/cpb.c20-00106. PMID: 32741913

[41] Francesca Orsola Alfano,Andrea Benassi, Roberto Gaspari, Alberto Di Renzo, Francesco Paolo Di Maio, *Full-Scale DEM Simulation of Coupled Fluid and Dry-Coated Particle Flow in Swirl-Based Dry Powder Inhalers*, ACS Publications, 2021, https://doi.org/10.1021/acs.iecr.1c02864

[42] R. Ponzini, R. Da Vià, S. Bnà, C. Cottini, A. Benassi, *Coupled CFD-DEM model for dry powder inhalers simulation: Validation and sensitivity analysis for the main model parameters*, Powder Technology 385, 2021, https://doi.org/10.1016/j.powtec.2021.02.044

[43] T. Forgber, J.G. Khinast, E. Fink, *A hybrid workflow for investigating wide DEM parameter spaces*, Powder Technology 404, 2022, https://doi.org/10.1016/j.powtec.2022.117440

[44] Dietmar Schulze, *Powders and Bulk Solids: Behavior, Characterization, Storage and flow Second Edition*, Springer,2007

Appendix A: Cyclone Design Concept

The air flow in a cyclone is mainly a swirling flow, creating the perfect mixing conditions for the powder. As shown in Figure A3, the gas inlet consists of two inputs, one vertical and one horizontal. The reason for this decision was the improved flow conditions and the efficient powder delivery in comparison with the device using only one of them. The comparison between the effects of different gas inlets on the flow regime was performed during setup calibration and exploration.

The behavior of the powder in the cyclone was approximated as powder flow through hoppers. The book by K. Kesava Rao and Prabhu R. Nott was studied [15] to obtain information on the parameters that affect the powder flowability through a silo. In their work, it is mentioned that the flow of powder-like materials through a hopper is not perfect. If the hopper is not well designed, the powder might not flow. The main reason for that is a phenomenon called "arching". When the powder starts flowing inside the conical shape, a percentage of it will be deposited on the walls and near the exit area. The reason the material is deposited in these regions is that these are stagnation regions; in other words, near the walls and the exit, there are areas where the velocity is zero, thus the particles cannot move. Once the particles stop moving, arches of particles might be formed. These arches are so strong that they will prevent the rest of the powder from flowing through. The arch formation is influenced by three main factors: the cohesive behavior of the powder, the wall friction angle, and the inclination angle of the hopper. In this project, we were able to change only the angle of the hopper, which also changed the wall friction angle. To properly study and improve the cyclone design, multiple numerical simulations would be run. Since this method would be incredibly time-consuming and computationally

demanding, it was decided to approach this problem by testing experimentally the effects of different cyclone angles and heights on the flow conditions. It was found that a blockage would appear in prototypes characterized by a steep angle or short active height, with the angle of inclination having a strong impact on powder flowability (see Figure A1). For the whole design testing procedure, a 3D printing process was followed to produce various geometries.

.

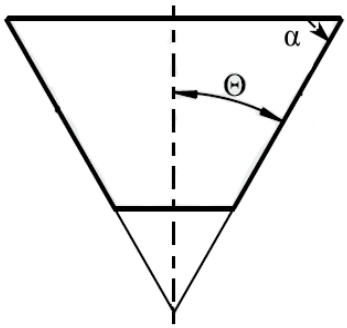

Figure A1: Cyclone wall inclination angle Θ in 2D geometry.

In addition to changing designs, different types of resin were also used to improve the surface quality of the cyclone. It was determined that the most crucial factor for a satisfying surface quality was the resin curing time. Models exposed to ultraviolet light for up to 5 min showed poor surface quality, meaning that more time was needed for proper treatment of the resin. More specifically, the surface would be sticky, which would greatly impact the adhesion of the particles on the wall. The designs were developed in a virtual environment using CAD commercial software, SolidWorks.

In Figure A2, all the dimensions are shown, but the most important ones that determine the cyclone efficiency are the height h = 76.88 mm and the radius r = 33.5 mm because they determine the angle of the cyclone, which in this case is $\alpha = 66.45^{o}$.

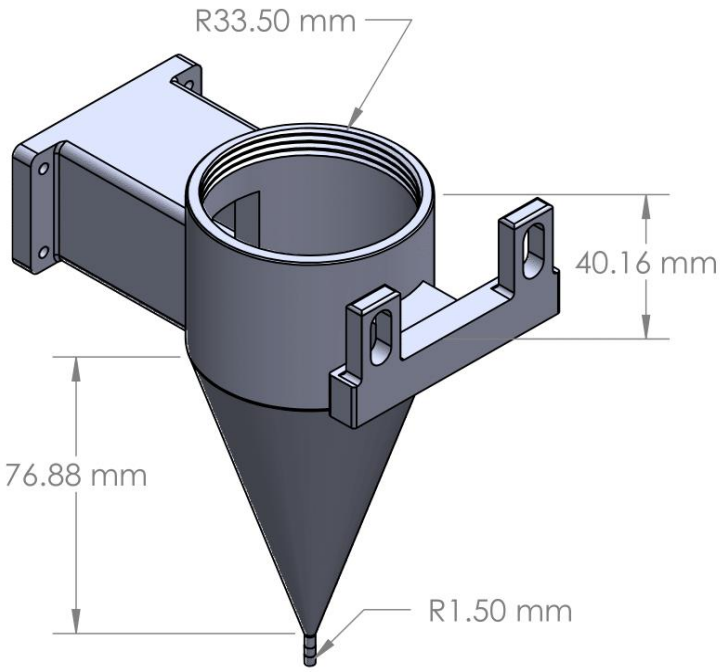

Figure A2: Cyclone main body dimensions: a) height h =76.88 mm b) radius r =33.5 mm.

Figure A3: Active cyclone lid geometry and dimensions.

Appendix B: Device Prototype Cost Analysis

The manufacturing process for the cyclone is meant to be simple and low-cost. The total cost to produce a prototype is shown in Table B1 below. It must be noted that the cost of the prototype is calculated to estimate the potential cost of the final product. For that reason, the pressure and flow rate regulators, as well as the cost of the pressure sensor, are not mentioned since they will not be part of it.

Table B1: Detailed cost calculation based on the materials and the equipment used for the prototype production.

Item #	Kind	Cost (CAD)	Manufacturer	Provider
1	Resin (100g)	10	Ministry of resin	Ministry of resin
2	Solenoid	22	Uxcell	Amazon
3	Arduino	46	Arduino	Arduino
4	Catheter	150	N/A	N/A
Total		**228**		

It must be noted that the total value does not represent the production cost. For example, to 3D print the whole geometry, 100 g of resin were needed, and the cost of the product that was used is 100 CAD per 1kg, so 10 CAD were needed for the main body of the device. Additionally, the cost of the catheter provided by our partners in the Kastrup Lab.